TESS Hunt for Young and Maturing Exoplanets (THYME). XI. An Earth-sized Planet Orbiting a Nearby, Solar-like Host in the 400 Myr Ursa Major Moving Group

Benjamin K. Capistrant[1], Melinda Soares-Furtado[2,3], Andrew Vanderburg[3], Alyssa Jankowski[2], Andrew W. Mann[4], Gabrielle Ross[5], Gregor Srdoc[6], Natalie R. Hinkel[7,8], Juliette Becker[2], Christian Magliano[9], Mary Anne Limbach[10], Alexander P. Stephan[11,12], Andrew C. Nine[2], Benjamin M. Tofflemire[13,27], Adam L. Kraus[13], Steven Giacalone[14], Joshua N. Winn[5], Allyson Bieryla[15], Luke G. Bouma[16,28], David R. Ciardi[17], Karen A. Collins[15], Giovanni Covone[9], Zoë L. de Beurs[18,29], Chelsea X. Huang[19], Jon M. Jenkins[20], Laura Kreidberg[21], David W. Latham[15], Samuel N. Quinn[15], Sara Seager[3,18,22], Avi Shporer[3], Joseph D. Twicken[23], Bill Wohler[23], Roland K. Vanderspek[3], Ricardo Yarza[24,25,30], and Carl Ziegler[26]

[1] Department of Astronomy, University of Florida, Bryant Space Science Center, Stadium Road, Gainesville, FL 32611, USA; bcapistrant@ufl.edu
[2] Department of Astronomy, University of Wisconsin-Madison, 475 N. Charter Street, Madison, WI 53706, USA; mmsoares@wisc.edu
[3] Department of Physics and Kavli Institute for Astrophysics and Space Research, Massachusetts Institute of Technology, Cambridge, MA 02139, USA
[4] Department of Physics & Astronomy, The University of North Carolina at Chapel Hill, Chapel Hill, NC 27599-3255, USA
[5] Department of Astrophysical Sciences, Princeton University, Princeton, NJ 08544, USA
[6] Kotizarovci Observatory, Sarsoni 90, 51216 Viskovo, Croatia
[7] Physics & Astronomy Department, Louisiana State University, Baton Rouge, LA 70803, USA
[8] Southwest Research Institute, San Antonio, TX 78238, USA
[9] Dipartimento di Fisica "Ettore Pancini,"Università di Napoli Federico II, I-80126 Napoli, Italy
[10] Department of Astronomy, University of Michigan, Ann Arbor, MI 48109, USA
[11] Department of Astronomy, The Ohio State University, Columbus, OH 43210, USA
[12] Center for Cosmology and AstroParticle Physics, The Ohio State University, Columbus, OH 43210, USA
[13] Department of Astronomy, The University of Texas at Austin, Austin, TX 78712, USA
[14] Department of Astronomy, 501 Campbell Hall #3411, University of California, Berkeley, Berkeley, CA 94720, USA
[15] Center for Astrophysics | Harvard & Smithsonian, 60 Garden Street, Cambridge, MA 02138, USA
[16] Department of Astronomy, MC 249-17, California Institute of Technology, Pasadena, CA 91125, USA
[17] Caltech/IPAC-NASA Exoplanet Science Institute, 770 S. Wilson Avenue, Pasadena, CA 91106, USA
[18] Department of Earth, Atmospheric and Planetary Sciences, Massachusetts Institute of Technology, Cambridge, MA 02139, USA
[19] University of Southern Queensland, Centre for Astrophysics, West Street, Toowoomba, QLD 4350 Australia
[20] NASA Ames Research Center, Moffett Field, CA 94035, USA
[21] Max Planck Institute for Astronomy, Königstuhl 17, D-69117 Heidelberg, Germany
[22] Department of Aeronautics and Astronautics, MIT, 77 Massachusetts Avenue, Cambridge, MA 02139, USA
[23] SETI Institute, Mountain View, CA 94043 USA/NASA Ames Research Center, Moffett Field, CA 94035 USA
[24] Department of Astronomy and Astrophysics, University of California, Santa Cruz, CA 95064, USA
[25] Texas Advanced Computing Center, University of Texas, Austin, TX 78759, USA
[26] Department of Physics, Engineering and Astronomy, Stephen F. Austin State University, 1936 North Street, Nacogdoches, TX 75962, USA

Abstract

Young terrestrial worlds are critical test beds to constrain prevailing theories of planetary formation and evolution. We present the discovery of HD 63433 d—a nearby (22 pc), Earth-sized planet transiting a young Sun-like star (TOI-1726, HD 63433). HD 63433 d is the third planet detected in this multiplanet system. The kinematic, rotational, and abundance properties of the host star indicate that it belongs to the young (414 ± 23 Myr) Ursa Major moving group, whose membership we update using new data from the third data release of the Gaia mission and TESS. Our transit analysis of the TESS light curves indicates that HD 63433 d has a radius of $1.1\,R_\oplus$ and closely orbits its host star with a period of 4.2 days. To date, HD 63433 d is the smallest confirmed exoplanet with an age less than 500 Myr, and the nearest young Earth-sized planet. Furthermore, the apparent brightness of the stellar host ($V \simeq 6.9$ mag) makes this transiting multiplanet system favorable to further investigations, including spectroscopic follow-up to probe the atmospheric loss in a young Earth-sized world.

Unified Astronomy Thesaurus concepts: Exoplanet systems (484)

---

[27] Joint first author.
[28] NASA Hubble Postdoctoral Fellow.
[29] 51 Pegasi b Fellow.
[30] NSF Graduate Research Fellow.
[31] MIT Presidential Fellow.
[32] NASA FINESST Fellow.
[33] Frontera Computational Science Fellow.

1. Introduction

The first few hundred million years after formation is a critical stage of the planetary lifecycle. At this early evolutionary stage, planets may thermally contract (e.g., Fortney et al. 2011) and experience significant atmospheric losses (e.g., Lammer et al. 2003; Lopez & Fortney 2013; Ginzburg et al. 2018). Moreover, the early phase of planetary system formation can be very dynamically active, particularly after the dissipation of the proto-planetary gas disk (e.g., Chambers & Wetherill 1998; Morbidelli et al. 2012). During the first tens of millions of years, young systems may be

susceptible to planet–planet scattering events (e.g., Fabrycky & Tremaine 2007; Chatterjee et al. 2008; Ford & Rasio 2008; Naoz et al. 2011), planet collisions (e.g., Asphaug et al. 2006; Hansen 2009), and the prolonged bombardment of planets by asteroids and planetesimals. Additionally, planetary systems in dense star-forming regions may undergo dynamical interactions with other stars in their natal clusters (e.g., Fregeau et al. 2006). Detailed observations of planetary systems in such environments are, therefore, crucial to understanding the general formation history of the exoplanet population.

Among the population of confirmed exoplanets with precisely measured age estimates, 50 exoplanets are estimated to be younger than 500 Myr. For context, we considered a system age estimate to be precisely measured if its error estimate is at most 50% of the estimated age value. Rarer still are young multiplanet systems with hosts bright enough to permit follow-up precision radial velocity investigations—only nine young multiplanet hosts are brighter than $G = 12$ mag.

In this paper, we report the detection and characterization of HD 63433 d—a young (414 ± 23 Myr), nearby (22.32 ± 0.06 pc) Earth-sized planet orbiting a Sun-like host (spectral type G5V). HD 63433 d is the third planet to be detected in this multiplanet system. The discovery of the other two HD 63433 planets, both mini Neptunes, was reported by Mann et al. (2020).

The discovery of young transiting exoplanets that are amenable to follow-up investigations is of critical importance, as such observations offer constraints to prevailing theoretical models of planetary formation and evolution. Because the planets in the HD 63433 system transit a bright ($V \simeq 6.9$ mag) host star, this system offers a good opportunity for follow-up analyses. This includes investigations of the transmission spectrum, stellar obliquity, and mass estimates derived via ground-based radial velocity data. The HD 63433 system has already been the subject of numerous follow-up studies thanks to its brightness and proximity (Dai et al. 2020; Zhang et al. 2022; Damasso et al. 2023; Mallorquín et al. 2023), and the newly detected HD 63433 d provides an additional opportunity for follow-up investigations, with the potential to offer constraints on the process of atmospheric escape in a young, Earth-sized exoplanet.

Our analysis of HD 63433 d is part of the TESS Hunt for Young and Maturing Exoplanets (THYME; Newton et al. 2019). The principal goal of THYME is the identification of young transiting exoplanets in moving groups, stellar associations, and open clusters. Stellar groups play an important role in this search, as they are comprised of stars that share common ages and compositions. Therefore, the ages of these systems may be determined using a combination of methods. The THYME project leverages the Transiting Exoplanet Survey Satellite (TESS; Ricker et al. 2015) light curves[34] of stellar members to search for the periodic brightness changes that are indicative of transiting exoplanets. For a review of the transit detection technique, we refer the reader to Santos (2008). The THYME project is the successor to the Zodiacal Exoplanets in Time Survey (ZEIT; Mann et al. 2016), which performed an analogous transiting exoplanet search using time series data from the K2 mission (a series of ecliptic-pointed campaigns conducted after the failure of the second reaction wheel of the Kepler satellite).

The following outline presents the organization of this manuscript. In Section 2, we present the data used in our analysis of HD 63433 and other members of the Ursa Major

Table 1
The Observation Specifications for Each of the TESS Sectors Analyzed in the Detection and Characterization of HD 63433 d

Sector	Cadence	Camera	CCD	Date Range
20	2 minutes	1	4	2019/12/24— 2020/01/20
44	20 s	4	1	2021/10/12— 2021/11/06
45	20 s	2	3	2021/11/06— 2021/12/02
46	20 s	1	3	2021/12/02— 2022/12/30
47	20 s	1	4	2021/12/30— 2022/01/28

moving group (hereafter referred to as UMa). In Section 3, we present the observed and inferred properties of HD 63433. In Section 4, we present our analysis of the transit signatures found in the TESS light curve of the host star. In this section, we also present our UMa membership analysis for the planet host, as well as the broader sample of likely UMa members. In Section 5, we describe the procedures we performed to assess false-positive scenarios for the HD 63433 d candidate. In Section 6, we present the results we obtained in our exoplanet characterization, as well as the results from our photometric rotational analyses. Finally, in Section 7, we present our summary and conclusions, highlighting some potential follow-up work.

2. Data

2.1. TESS Photometry

2.1.1. The HD 63433 TESS Light Curve

TESS observations are divided into individual sectors. Each sector is observed continuously for approximately 27 days and covers a region $24° \times 96°$ in size. To date, HD 63433 has been observed in five distinct TESS sectors, resulting in an irregularly sampled baseline that spans between 2019 December 24 and 2022 January 28. In Table 1, we list the sectors, camera numbers, CCD numbers, and sector-specific date ranges that correspond to each observation.

To analyze the HD 63433 time series and search for exoplanetary signals, we leveraged data from all five TESS sectors; the image data were reduced and analyzed by the Science Processing Operations Center at NASA Ames Research Center (Jenkins et al. 2016). It has been shown that 20 s cadence data have better photometric precision than 2 minute cadence data (Huber et al. 2022). Therefore, we used 20 s cadence data when they were available, opting for 2 minute cadence data otherwise. Also, in our experience, a custom systematics correction can often yield improved results over the default TESS pipeline light curves, especially for young stars with high-amplitude stellar variability. We performed a bespoke analysis, starting with the simple aperture photometry (Twicken et al. 2010; Morris et al. 2020) light curves generated by the TESS Science Processing Operations Center (SPOC) pipeline.[35] The SPOC data described in this section can be found in MAST: doi:10.17909/t51r-sh87.

We applied systematic corrections to these light curves, following the procedure outlined by Vanderburg et al. (2019) and briefly summarized here. The SPOC light curves were fit with a linear model, which consisted of the following components:

1. a basis spline (B-spline) with regularly spaced breaks at 0.3 day intervals to model signatures of low-frequency stellar variability,
2. the mean and standard deviation of the spacecraft quaternion time series within each light-curve exposure,[36]
3. seven cotrending vectors from the SPOC Presearch Data Conditioning's band 3 (fast timescale) flux time series correction with the largest eigenvalues (Smith et al. 2012; Stumpe et al. 2012, 2014),
4. a high-pass-filtered (0.1 day) flux time series from the SPOC background aperture.

No flares were observed in the data. Leveraging the systematics-corrected light curves for all five TESS sectors, we searched for transit signals using a box-least-squares (BLS) periodogram (Kovács et al. 2002). This methodology is described in more detail in Vanderburg et al. (2016). We detected the transiting signatures of exoplanets HD 63433 b and HD 63433 c at high significance. Both HD 63433 b and c were detected by the Science Processing Operations Center (Jenkins et al. 2016) at NASA Ames Research Center on 2020 February 2, and the TESS Science Office issued alerts for these candidates on 2020 February 19 and 20, respectively (Guerrero et al. 2021). Mann et al. (2020) first reported the discovery of these planets using a single sector of TESS data (Sector 20). After removal of those two signals, we detected for the first time a third transit signature with a period of 4 days and a shallower transit depth than the signatures of HD 63433 b and HD 63433 c. We additionally apply this process using the transit least squares (TLS) algorithm (Hippke & Heller 2019), which incorporates features such as stellar limb-darkening and the effects of planetary ingress and egress. We recover the third transit signature using this algorithm, and, as found with our BLS search, see no additional periodic signals after removing all three transits from the light curve.

We attribute this signal to a new planet called HD 63433 d. The transit depth of HD 63433 d is about 100 ppm, consistent with that of an Earth-sized planet. The new signal was not reported by either the TESS SPOC or MIT Quick Look Pipeline (Huang et al. 2020a, 2020b) transit searches and was not listed as a TESS planet candidate. We found that the HD 63433 d transit signal was too shallow to be detected with a single sector of TESS data, which is likely why it escaped detection in Mann et al. (2020). Nevertheless, this transit signal is clearly detectable in our analysis of the full, five-sector light curve, with a signal-to-noise ratio (S/N) of about 15.

We performed the standard battery of tests to assess whether the origin of the signal is indeed planetary in nature. This includes an inspection of the phase-folded light curve, tests for consistency of even/odd transits, and a search for secondary eclipses. We found no evidence to refute the detection of HD 63433 d and proceed under the assumption that this signal is a viable planet candidate. We also performed a difference

image centroid offset analysis (Twicken et al. 2018) using the SPOC data validation pipeline software and found that the signal must originate within about 20″ of HD 63433, corroborating this interpretation.

After producing our final light curve, we flattened it by simultaneously fitting the three transit signals along with a variability model, similar to the methods used by Vanderburg et al. (2016, albeit without also simultaneously fitting for systematic errors), Pepper et al. (2020). We use this flattened light curve in our Markov Chain Monte Carlo (MCMC) analysis, as described in Section 1.

2.1.2. Light Curves for Other Ursa Major Candidate Members

In addition to kinematic analysis, another important method in distinguishing moving group membership is the analysis of the main-sequence candidate population's gyrochronological rotation sequence, as coeval stars will map out a relation between color and rotation period whose slope is dependent upon the cluster age. We refer the interested reader to Meibom et al. (2011) for a more in-depth discussion of this topic. Candidate UMa members were identified in a volume-limited search (50 pc radius) of HD 63433 and further assessed for membership using the process described in Section 4.2.

To measure photometric rotation periods of UMa candidates, we extracted TESS light curves for each target using cutouts of the full frame images (30 minutes cadence data for the first 2 yr of observations, 10 minutes cadence for the third and fourth years of observations, and 200 s cadence for the fifth and sixth years of observations) via TESSCUT[37] (Brasseur et al. 2019). The light curves were extracted using 20 apertures, and then, we performed a systematic correction process similar to that described in Section 2.1.1 on each light curve. For each source, we identified the aperture that produced the light curve with the highest photometric precision. All light curves were normalized and σ clipped using a 3.5σ threshold. We then analyzed these light curves to search for photometric rotation periods, a process we describe further in Section 4.2.

2.2. Archival Spectroscopy

As a nearby, bright, young star, HD 63433 has been the subject of numerous spectroscopic investigations over the decades, and a treasure trove of archival high-resolution spectroscopic observations of the star exists. Mann et al. (2020) gathered archival radial velocity observations from the ELODIE (Baranne et al. 1996), SOPHIE (Perruchot et al. 2008), and Lick Hamilton spectrographs (Fischer et al. 2014), and collected their high-resolution spectra from the Tillinghast Reflector Echelle Spectrograph (TRES; Fűrész 2008) and the Network of Robotic Echelle Spectrogaphs (NRES; Siverd et al. 2018). Since the discovery of the two large planets in the system, new spectroscopic observations from the High Accuracy Radial velocity Planet Searcher for the Northern hemisphere (HARPS-N; Damasso et al. 2023) and CARMENES (Mallorquín et al. 2023) have been added to this extensive list. Tabulated versions of the radial velocity observations used in this investigation can be found in Table 2 of Mann et al. (2020), Table D.1 of Damasso et al. (2023), and Tables C.1 and C.2 of Mallorquín et al. (2023). All of these data show no large radial velocity (RV) signals corresponding

---

[36] The quaternion measurements are 2 s cadence vector time series that describe the spacecraft orientation in relation to guide star observations. TESS quaternions are available at https://archive.stsci.edu/missions/tess/engineering/.

[37] TESSCUT: https://mast.stsci.edu/tesscut/.

to stellar-mass companions, which allows us to rule out a variety of false-positive scenarios for our newly detected planet candidate (see Section 5).

2.3. Ground-based Seeing-limited Photometry

Signals from blended eclipsing binaries can sometimes result in false-positive transit signals—a concern that is exacerbated by the large pixel size of the TESS instrument (21″ per pixel). To rule out such false-positive scenarios for HD 63433 d, we observed the star during the predicted time of transit for the new planet candidate using the Las Cumbres Observatory Global Telescope (LCOGT; Brown et al. 2013) 1 m telescope at McDonald Observatory on 2022 February 24. The observations were conducted with the 4096×4906 pixel Sinistro cameras in Sloan z band. The data were reduced by the LCO BANZAI pipeline (McCully et al. 2018). The light curves were extracted using AstroImageJ (Collins et al. 2017) using an aperture radius of 2″.5. No sources within this distance were identified with adaptive optics (AO) imaging or in the third data release of the Gaia mission (Gaia DR3) data. While the photometric precision of the target star's light curve was insufficient to detect the shallow transits observed by TESS, the observations showed no evidence of eclipses or other variability in the nearby stars that could be responsible for the signal associated with HD 63433 d (down to $G_{\mathrm{Gaia}} = 19$ mag). For reference, the closest star to our target is a $G_{\mathrm{Gaia}} = 19$ mag star at an angular separation of 18″. The 2022 February 24 data firmly rule out North Equatorial Belts in stars within 2′.5 of the target over a -24.3σ to $+22.2\sigma$ observing window. All ground-based follow-up light curves are available on ExoFOP.[38]

2.4. Seeing-limited Archival Photometry

To corroborate the nondetection of variability of any stars close to the position of HD 63433, we used archival ground-based photometric data from the Zwicky Transient Facility (ZTF) survey (Masci et al. 2019) to check whether the HD 63433 d 4 days transit signal might be the result of a blended eclipsing binary. We used the `DEATHSTAR` software package (Ross et al. 2023) to download ZTF image cutouts of the sky surrounding HD 63433 and extract light curves from all the stars within 2′.5 of the target. We folded the light curves of each nearby star (8 in total) on the orbital period of HD 63433 d and ruled out variability that could plausibly cause the transit signal we see in TESS from any stars other than HD 63433. We conclude that the signal must be coming from HD 63433, consistent with the planetary interpretation.

2.5. Archival Adaptive Optics Imaging

To verify the first two exoplanet detections in the HD 63433 system, Mann et al. (2020) collected archival adaptive optics imaging data spanning nearly a decade (1999–2008, Mason et al. 2001; Raghavan et al. 2012), none of which showed any evidence for bound companions, or any background sources bright enough to cause the transit signals. Combining the detection limits from these archival adaptive optics observations with stellar evolutionary models from Baraffe et al. (2015) based on an inferred system age of 400 Myr, Mann et al. (2020) ruled out the presence of background sources down to substellar masses. We verified this with our own high-angular-

---

resolution observations: an AO observation from Keck Observatory using the NIRC2 instrument on 2020 September 9 in a narrow Brγ filter, and a speckle observation from the Southern Astrophysics Research telescope with the HRCam instrument on 2020 December 29. For reference, the Keck AO observation has the following parameters: an estimated pixel scale of 0″.009942, point-spread function (PSF) of 0″.0496482, and an estimated contrast of 7.310 mag at 0″.5. Similarly, the speckle observations have the following parameters: an estimated pixel scale of 0″.01575, PSF of 0″.06364, and an estimated contrast of 7.6 mag at 1″. Neither of these observations showed any new evidence for nearby companions or background objects capable of producing the transit signatures of HD 63433 d.

2.6. Gaia DR3 Data

We utilized Gaia DR3 (Gaia Collaboration et al. 2021) to investigate the kinematic properties, spatial distribution, and stellar properties of HD 63433 and a population of candidate UMa members. The candidate UMa members were identified and assessed for membership using the processes described in Section 4.2. Gaia magnitudes, colors, parallaxes, extinction values, and reddening constraints were employed to determine the properties of this population of targets.

2.7. Archival Lithium Abundances

The published lithium abundance measurements for HD 63433, and the identified UMa catalog sources are drawn from the following catalogs: Soderblom et al. (1993), King & Schuler (2005), Mishenina et al. (2008), Ammler-von Eiff & Guenther (2009), Gonzalez et al. (2010), Ramírez et al. (2012), Luck (2017), Aguilera-Gómez et al. (2018), and Llorente de Andrés et al. (2021). We found that fewer than 20% of our catalog members had corresponding lithium abundance measurements in the literature.

3. Host Star Properties

3.1. Properties of the Host Star

HD 63433 is a well-studied star thanks to its proximity to Earth and long-suspected membership of the Ursa Major moving group, and was thoroughly characterized by Mann et al. (2020). Since that work, an updated parallax from Gaia DR3 has been released, but the change does not appreciably impact the stellar parameters, so we simply adopt the stellar parameters from Mann et al. (2020) for the rest of this work. The directly observed and inferred properties of the host star HD 63433 (TIC 130181866, TOI 1726, HIP 38228, Gaia DR3 875071278432954240) are shown in Table 2, and the abundance properties are provided in Table 3 (from the Hypatia Catalog, Hinkel et al. 2014).

Most notably, HD 63433 is bright ($V \simeq 6.9$ mag), young (414 ± 23 Myr), and positioned at a close distance from the Earth (22.32 ± 0.06 pc). Additionally, HD 63433 is a solar analog (spectral type G5V), exhibiting solar-like qualities, including a mass of $0.99 \pm 0.03 \, M_{\odot}$ and [Fe/H] $= 0.03 \pm 0.05$ dex (Hinkel et al. 2014). Due to the youth of the host star, it differs substantially from the Sun in terms of its strong lithium abundance (A(Li) $= 2.5 \pm 0.2$ dex), short rotation period ($P_{\mathrm{rot}} = 6.4 \pm 0.6$ days), and high X-ray luminosity ($L_X/L_{\mathrm{bol}} = 0.75 \pm 0.03$).

Table 2
Properties of the Host Star HD 63433

Parameter	Value	Source
TIC ID	130181866	TESS Input Catalog
TOI ID	1726	Guerrero et al. (2021)
Gaia DR3 ID	875071278432954240	Gaia DR3
Astrometry		
α.	07:49:55.048	Gaia DR3
δ.	+27:21:47.28	Gaia DR3
μ_α	-10.220 ± 0.022	Gaia DR3
μ_δ (mas yr^{-1})	-11.235 ± 0.014	Gaia DR3
π (mas)	44.6848 ± 0.0228	Gaia DR3
distance (pc)	22.32 ± 0.06	Gaia DR3
Photometry		
Spectral Type	G5V	Gray et al. (2003)
$G_{\rm Gaia}$ (mag)	6.7372 ± 0.0028	Gaia DR3
$BP_{\rm Gaia}$ (mag)	7.0763 ± 0.0034	Gaia DR3
$RP_{\rm Gaia}$ (mag)	6.2228 ± 0.0042	Gaia DR3
B_T (mag)	7.749 ± 0.016	Tycho-2
V_T (mag)	6.987 ± 0.010	Tycho-2
J (mag)	5.624 ± 0.043	2MASS
H (mag)	5.359 ± 0.026	2MASS
Ks (mag)	5.258 ± 0.016	2MASS
W1 (mag)	5.246 ± 0.178	ALLWISE
W2 (mag)	5.129 ± 0.087	ALLWISE
W3 (mag)	5.297 ± 0.016	ALLWISE
W4 (mag)	5.163 ± 0.031	ALLWISE
Kinematics and Galactic Position		
$RV_{\rm Bary}$ (km s^{-1})	-16.07 ± 0.13	Gaia DR3
U (km s^{-1})	13.88 ± 0.09	This paper
V (km s^{-1})	2.49 ± 0.02	This paper
W (km s^{-1})	-7.87 ± 0.04	This paper
X (pc)	-19.84 ± 0.03	This paper
Y (pc)	-4.68 ± 0.01	This paper
Z (pc)	9.14 ± 0.01	This paper
Physical Properties		
$P_{\rm rot}$ (days)	6.4 ± 0.6	This paper
$L_X/L_{\rm bol}$	$(9.1 \pm 2.7) \times 10^{-5}$	Mann et al. (2020)
$\log R'_{\rm HK}$	-4.39 ± 0.05	Mann et al. (2020)
$v \sin i$ (km s^{-1})	7.26 ± 0.15	Mallorquín et al. (2023)
$i_\star$ ($^\circ$)	>71	Mann et al. (2020)
Age (Myr)	414 ± 23	Jones et al. (2015)
$T_{\rm eff}$ (K)	5688 ± 28	Hinkel et al. (2014)
$M_\star$ ($M_\odot$)	0.99 ± 0.03	Mann et al. (2020)
$R_\star$ ($R_\odot$)	0.912 ± 0.034	Mann et al. (2020)
$L_\star$ ($L_\odot$)	0.75 ± 0.03	Mann et al. (2020)
$\rho_\star$ ($\rho_\odot$)	1.3 ± 0.2	Mann et al. (2020)
$\log(g)$ ($\log(\mathrm{cm\,s}^{-2})$)	4.52 ± 0.05	Hinkel et al. (2014)

Table 3
Abundance Properties of HD 63433

Parameter	Value
[Fe/H] (dex)	0.03 ± 0.05
A(Li) (dex)	2.5 ± 0.2
[C/H] (dex)	-0.09 ± 0.074
[N/H] (dex)	-0.22 ± 0.11
[O/H] (dex)	0.00 ± 0.014
[Na/H] (dex)	-0.08 ± 0.24
[Mg/H] (dex)	0.02 ± 0.19
[Al/H] (dex)	-0.05 ± 0.19
[Si/H] (dex)	-0.03 ± 0.08
[SiII/H] (dex)	0.05 ± 0.05
[S/H] (dex)	0.18 ± 0.09
[Ca/H] (dex)	0.09 ± 0.086
[CaII/H] (dex)	0.56 ± 0.03
[Sc/H] (dex)	0.15 ± 0.067
[ScII/H] (dex)	0.08 ± 0.09
[Ti/H] (dex)	0.03 ± 0.17
[TiII/H] (dex)	0.13 ± 0.06
[V/H] (dex)	0.00 ± 0.094
[VII/H] (dex)	0.06 ± 0.11
[Cr/H] (dex)	0.04 ± 0.094
[CrII/H] (dex)	-0.24 ± 0.07
[Mn/H] (dex)	-0.15 ± 0.16
[Co/H] (dex)	0.07 ± 0.04
[Ni/H] (dex)	-0.04 ± 0.10
[Zn/H] (dex)	-0.34 ± 0.16
[Zr/H] (dex)	0.28 ± 0.10
[PrII/H] (dex)	0.31 ± 0.10
[Eu/H] (dex)	-0.04 ± 0.11
[EuII/H] (dex)	-0.04 ± 0.28

Note. All values were obtained using the Hypatia Catalog. We report only sources with errors less than 0.3 dex (Hinkel et al. 2014).

(SED) using a grid of empirical templates (with atmosphere models to fill in wavelength gaps). The method provides two estimates of $R_\star$, one from the Stefan–Boltzmann relation (using the Gaia DR3 parallax and bolometric flux from the SED) and another from the infrared-flux method (Blackwell & Shallis 1977), i.e., from the scale factor between the absolutely calibrated spectrum and the model spectrum. Both radii agree, and both methods reproduce radii from long-baseline interferometry (e.g., von Braun et al. 2012). The resulting $T_{\rm eff}$ and R_* are within 1σ of those reported from Gaia DR3 (Gaia Collaboration 2022). The stellar radius uncertainty from Mann et al. (2020) was only propagated along with the mass uncertainty for the starting parameter for stellar density, but $R_{\rm p}/R_\star$ was a separate parameter that had its own value and uncertainty also determined from the transit models in Mann et al. (2020).

4. Analysis

4.1. Transit Analysis and Results

We used the easy differential-evolution Markov Chain Monte Carlo algorithm, edmcmc (Vanderburg 2021),[39] to obtain transit-fit parameters and uncertainties for the three planets in the HD 63433 system (Ter Braak 2006). The method involves generating many possible solutions, or model

The Galactic space velocity values were calculated using PyAstronomy tools that draw from the methodology described in Johnson & Soderblom (1987). These calculations relied on Gaia DR3 kinematic and positional measurements. The spatial center of the UMa moving group is $(X, Y, Z) = (-7.5, +9.9, +21.9)$ pc (Gagné et al. 2018). This can be compared to the Cartesian Galactic coordinates of HD 63433, measured as $(x', y', z') = (-19.89, -4.70, +9.16)$ pc. We determined that HD 63433 is approximately 23 pc the central point of the UMa moving group. This is similar to the Earth-HD 63433 distance, but in the opposite direction, making HD 63433 roughly equidistant between the solar system and UMa core. This estimate is in good agreement with the value determined in Mann et al. (2020).

Our analysis incorporates stellar properties determined by Mann et al. (2020). They fit the spectral energy distribution

---

[39] https://github.com/avanderburg/edmcmc

Table 4
$\mathcal{U}[X, Y]$ Indicates a Uniform Prior with Limits X and Y, and $\mathcal{N}[X, Y]$ Indicates a Gaussian Prior with Mean X, and Standard Deviation Y

Parameter	Prior
T_0 (TJD)	$\mathcal{U}[-\infty, \infty]$
P (days)	$\mathcal{U}[0, \infty]$
$R_P/R_\star$	$\mathcal{U}[0, 1]$
b	$\mathcal{U}[|b| < 1 + R_P/R_*]$
$\rho_\star$ ($\rho_\odot$)	$\mathcal{N}[1.312, 0.152]$
$q_{1,1}$	$\mathcal{N}[0.30, 0.06]$
$q_{2,1}$	$\mathcal{N}[0.37, 0.05]$
$\sqrt{e} \sin\omega$	$\mathcal{U}[-1, 1]$
$\sqrt{e} \cos\omega$	$\mathcal{U}[-1, 1]$

parameters, that describe the light-curve transit signal. These parameters are sampled from a probability distribution using the MCMC technique. This technique helps to ensure that the chain explores the full parameter space and prevents the algorithm from getting stuck at local minima.

We then employed the BAsic Transit Model cAlculatioN `Python` package (`BATMAN`; Kreidberg 2015), producing three transit models that the `edmcmc` then fit simultaneously. For reference, `BATMAN` requires inputs for the following variables: time of inferior conjunction (T_0), planet orbital period (P), planet-to-star radius ratio (R_p/R_*), inclination (i), argument of periastron (ω), eccentricity (e), limb-darkening coefficients (described below), and scaled semimajor axis ($a/R_\star$).

To reduce the number of input parameters into the `edmcmc`, each planet's semimajor axis ($a/R_\star$) was calculated by leveraging Kepler's third law (under the assumption that $M_{\rm p}/M_\star \ll 1$),

$$\frac{a}{R_\star} = \sqrt[3]{\frac{GP^2\rho_*}{3\pi}}, \tag{1}$$

where G is the gravitational constant, P is the orbital period, and ρ_* is the mean stellar density. This allowed us to replace the orbital separations of individual planets with a single free parameter (the mean stellar density). We also reparameterized the eccentricity and argument of periastron for each planet as $\sqrt{e} \sin(\omega)$ and $\sqrt{e} \cos(\omega)$, which has been shown to improve MCMC convergence. We also fit for linear and quadratic limb-darkening coefficients (u_1, u_2), which we fit for using the (q_1, q_2) parameterization described by Kipping (2013). In order to interface with `BATMAN`, which calculates models in terms of u_1 and u_2, we solved for these coefficients using the following transformations:

$$u_1 = 2\sqrt{q_1}\, q_2; \tag{2}$$

$$u_2 = \sqrt{q_1}(1 - 2q_2), \tag{3}$$

as determined by Kipping (2013).

For our `edmcmc` analysis, we imposed Gaussian priors on the mean stellar density and limb-darkening coefficients. The priors imposed on the limb-darkening coefficients are the same as those used by Mann et al. (2020). The width of the stellar density prior was found via error propagation using the stellar mass ($M_\star$) and radius ($R_\star$) uncertainties calculated by Mann et al. (2020) after our derivation of the parameter. Other parameters are sampled uniformly, some using physically motivated constraints, such as the optimal impact parameter (b) for each planet being constrained to $|b| < 1 + R_P/R_\star$,

$R_p/R_\star > 0$, and $\sqrt{e}\cos\omega$ and $\sqrt{e}\sin\omega$ were restricted to $(-1, 1)$. Lastly, we restricted the eccentricity of the three planet orbits to be $e < 0.9$, because high values of eccentricity can sometimes lead to failures of `BATMAN`'s Kepler equation solver. This did not appreciably impact the posterior probability distributions for eccentricity, as the transit data were sufficient to constrain the eccentricity to be less than this value. The priors implemented for all three planets are listed in Table 4.

Key parameters in the `edmcmc` code include the number of walkers (the number of individual chains), the number of links (the number of steps that an individual chain will take), and the number of burn-in steps. For context, the number of burn-in steps represents the number of cycles in the initial portion of the MCMC chain that is to be discarded, as the algorithm has yet to reach equilibrium and could bias the evolution of the posterior distribution. Each run of the `edmcmc` code returns an object, which contains the positions of each walker at each link.

We initialized the MCMC chains at parameters near the values reported for HD 63433 b and HD 63433 c by Mann et al. (2020). In contrast, we initialized the parameters for HD 63433 d based on a by-eye inspection of the BLS power spectrum and phase-folded light curve of the period corresponding to the strongest peak in the power spectrum. Given that transiting exoplanets exhibit a near-edge on inclination, we set the initial inclination input for HD 63433 d to 90°.

For our initial run, the eccentricity (e) and argument of periastron (ω) were fixed to 0. By running our model with $e = \omega = 0$, we simplify our procedure by reducing the number of free parameters to be explored. This initial run with $e = \omega = 0$ employed 10^2 walkers, 5×10^4 links, and 10^3 burn-in steps. We utilize the well-converged results from this run as the initial positions for our subsequent runs, where e and ω were then incorporated as free variables. For these runs that explore a larger parameter space, we employ 10^2 walkers, 10^6 links, and 10^4 burn-in steps.

To determine if the `edmcmc` code has converged to the true posterior distribution of our system, we employed the Gelman & Rubin (1992) convergence statistic. For reference, a Gelman–Rubin value near unity (largest value of 1.2) for each parameter is an indicator that convergence has been achieved. To improve upon the convergence of our first run, we incorporated the results from this run as the starting position for a second run with 10^6 links. We repeated this process without applying burn-in steps for the successive runs, as the starting positions are taken from the preceding runs. We were ultimately satisfied with the convergence of the posterior distribution parameters after repeating this step seven times, resulting in a combined chain of seven million links. We then used our well-converged `edmcmc` outputs to construct transit models for each of the three detected HD 63433 planets, once again employing the `BATMAN` package.

The resulting best-fit parameters and uncertainties from our `edmcmc` investigation are listed in Table 5. Figure 1 depicts the unflattened HD 63433 TESS light curve (top panel), the flattened light curve with the three `BATMAN` transit models overlaid (middle panel), and the phase-folded light curves and transit models for the three planets (bottom panel). These results are discussed further in Section 6.

4.2. Association of HD 63433 with Ursa Major Moving Group

HD 63433 was previously determined to be a likely member of the UMa moving group via an analysis of kinematics, lithium

Table 5
Transit-fit Parameters

Parameter	Planet B	Planet C	Planet D	Planet B	Planet C	Planet D
		e,ω Fixed			e,ω Free	
			Transit-fit Parameters			
T_0 (TJD)	1916.45286 ± 0.00042	$1844.05971^{+0.00052}_{-0.00051}$	$2373.82337^{+0.00104}_{-0.00073}$	$1916.45262^{+0.00062}_{-0.00065}$	$1844.05971^{+0.00060}_{-0.00057}$	$2373.82345^{+0.00113}_{-0.00073}$
P (days)	7.1079342 ± 0.0000049	20.543784 ± 0.000016	$4.209078^{+0.000016}_{-0.000022}$	7.1079379 ± 0.0000054	$20.543791^{+0.000017}_{-0.000018}$	$4.209075^{+0.000012}_{-0.000023}$
$R_P/R_\star$	0.02116 ± 0.00011	$0.02578^{+0.00014}_{-0.00013}$	0.01090 ± 0.00016	$0.02123^{+0.00050}_{-0.00034}$	$0.02534^{+0.00033}_{-0.00026}$	$0.01079^{+0.00022}_{-0.00018}$
$\rho_\star$ ($\rho_\odot$)		$1.11^{+0.18}_{-0.21}$			1.27 ± 0.19	
$q_{1,1}$		$0.150^{+0.027}_{-0.024}$			$0.212^{+0.029}_{-0.026}$	
$q_{2,1}$		$0.0046^{+0.0076}_{-0.0034}$			$0.382^{+0.048}_{-0.047}$	
$\sqrt{e}\sin\omega$	0 (fixed)	0 (fixed)	0 (fixed)	$0.29^{+0.18}_{-0.25}$	$-0.08^{+0.26}_{-0.21}$	$0.14^{+0.23}_{-0.19}$
$\sqrt{e}\cos\omega$	0 (fixed)	0 (fixed)	0 (fixed)	$0.0023^{+0.4767}_{-0.4680}$	$-0.0084^{+0.5822}_{-0.5520}$	$-0.0038^{+0.4865}_{-0.4709}$
i (°)	$88.71^{+0.49}_{-0.44}$	$88.98^{+0.11}_{-0.13}$	$88.26^{+0.83}_{-0.66}$	$88.49^{+0.87}_{-0.40}$	$89.28^{+0.40}_{-0.22}$	$88.73^{+0.85}_{-1.06}$
			Derived Parameters			
$a/R_\star$	$16.08^{+0.58}_{-0.72}$	$32.6^{+1.2}_{-1.5}$	$11.34^{+0.41}_{-0.51}$	$16.83^{+0.57}_{-0.63}$	$34.15^{+1.16}_{-1.29}$	$11.87^{+0.40}_{-0.45}$
b	$0.31^{+0.11}_{-0.13}$	0.56 ± 0.05	$0.31^{+0.11}_{-0.16}$	$0.38^{+0.09}_{-0.21}$	$0.37^{+0.14}_{-0.21}$	0.23 ± 0.16
T_{14} (days)	$0.13422^{+0.00045}_{-0.00041}$	$0.16883^{+0.00073}_{-0.00061}$	$0.1118^{+0.0013}_{-0.0022}$	$0.122^{+0.012}_{-0.012}$	$0.171^{+0.013}_{-0.014}$	$0.1077^{+0.0056}_{-0.0149}$
T_{23} (days)	$0.12801^{+0.00042}_{-0.00047}$	$0.15655^{+0.00060}_{-0.00073}$	$0.1091^{+0.0013}_{-0.0023}$	0.115 ± 0.012	$0.161^{+0.014}_{-0.013}$	$0.105^{+0.006}_{-0.015}$
e	0 (fixed)	0 (fixed)	0 (fixed)	$0.24^{+0.27}_{-0.18}$	$0.21^{+0.33}_{-0.14}$	$0.16^{+0.36}_{-0.12}$
R_p ($R_\oplus$)[1]	2.105 ± 0.079	2.565 ± 0.097	1.084 ± 0.043	$2.112^{+0.093}_{-0.086}$	2.521 ± 0.1	$1.073^{+0.046}_{-0.044}$
a (AU)	$0.0682^{+0.0035}_{-0.0040}$	$0.1382^{+0.0072}_{-0.0082}$	$0.0481^{+0.0025}_{-0.0028}$	$0.0714^{+0.0036}_{-0.0038}$	$0.1448^{+0.0073}_{-0.0077}$	$0.0503^{+0.0025}_{-0.0027}$

Note.
[a] R_p derived using the R_* value from Table 2.

abundance, and stellar rotation (Mann et al. 2020). Now, with the release of Gaia DR3, it is possible to better characterize the Ursa Major moving group, identify new likely members, and assess whether HD 63433's membership remains solid. Therefore, we perform a moving group membership analysis, drawing from a volume-limited candidate population of UMa members. In this section, we describe the candidate member identification process and the methods used to cull this candidate list down to likely members. We note that, while other groups have also investigated the membership of Ursa Major using Gaia data (e.g., Gagné et al. 2020), we choose to perform our own identification of possible sources for consistency.

4.2.1. Identifying UMa Candidates

To identify a volume-limited population of comoving stellar companions for the HD 63433 target, our team employed the open-source Python tool Comove[40] (Tofflemire et al. 2021). The software identifies comoving sources with the procedure outlined below.

1. The software queries the Gaia DR3 catalog drawing targets from a volume radius equivalent to the defined search sphere ($r = 50$ pc in our case), and with tangential velocities (drawing from the target's proper motion) within a specified input velocity difference range (± 5 km s^{-1} in our case).
2. The software queries the Two Micron All Sky Survey (2MASS), Galaxy Evolution Explorer (GALEX), ROSAT, and Wide-field Infrared Survey Explorer (WISE) catalogs, recording measurements for the identified kinematic companions.
3. The software outputs a table listing parameters corresponding to the candidate population. Among the parameters reported are the following: the observed radial

velocity from Gaia DR3 (when available), the radial velocity value predicted if the source were comoving with the target with the given tangential velocities, the angular/linear separation between a given source and the target, and Gaia DR3 renormalized unit weight error (RUWE), which can be used to flag for potential binary companions (e.g., Evans 2018; Rizzuto et al. 2018; Belokurov et al. 2020).

Comove derived a table of 1180 potential comoving candidates. We then culled this table to only include sources with reported Gaia DR3 radial velocity measurements that were within ± 5 km s^{-1} of Comove-predicted value. This step resulted in the greatest removal of targets, bringing our table of potential comoving candidates down to 290 sources. It is important to note that 407 of the original candidates did not possess reported Gaia DR3 radial velocity measurements, due to the faintness and brightness limitations of the current radial velocity survey. This limited UMa candidates to a population of main-sequence stars spanning masses of 0.2–1.5 $M_\odot$, as determined by PAdova and TRieste Stellar Evolution Code (PARSEC, version 1.2S; Bressan et al. 2012). The sources removed at this step warrant further study if/when radial velocity measurements are made available. Next, we removed sources that have not yet been observed by TESS, further reducing our table of potential comoving candidates to 130 sources.

4.2.2. Measuring Photometric Rotation Periods for HD 63433 and Our UMa Candidates

We investigated the photometric rotation periods for all 130 UMa candidates. To determine the best period corresponding to a given target, each source was analyzed using three period-search techniques. This included a Lomb–Scargle (LS) periodogram analysis (Lomb 1976; Scargle 1982; Zechmeister & Kürster 2009); the phase dispersion minimization (PDM)
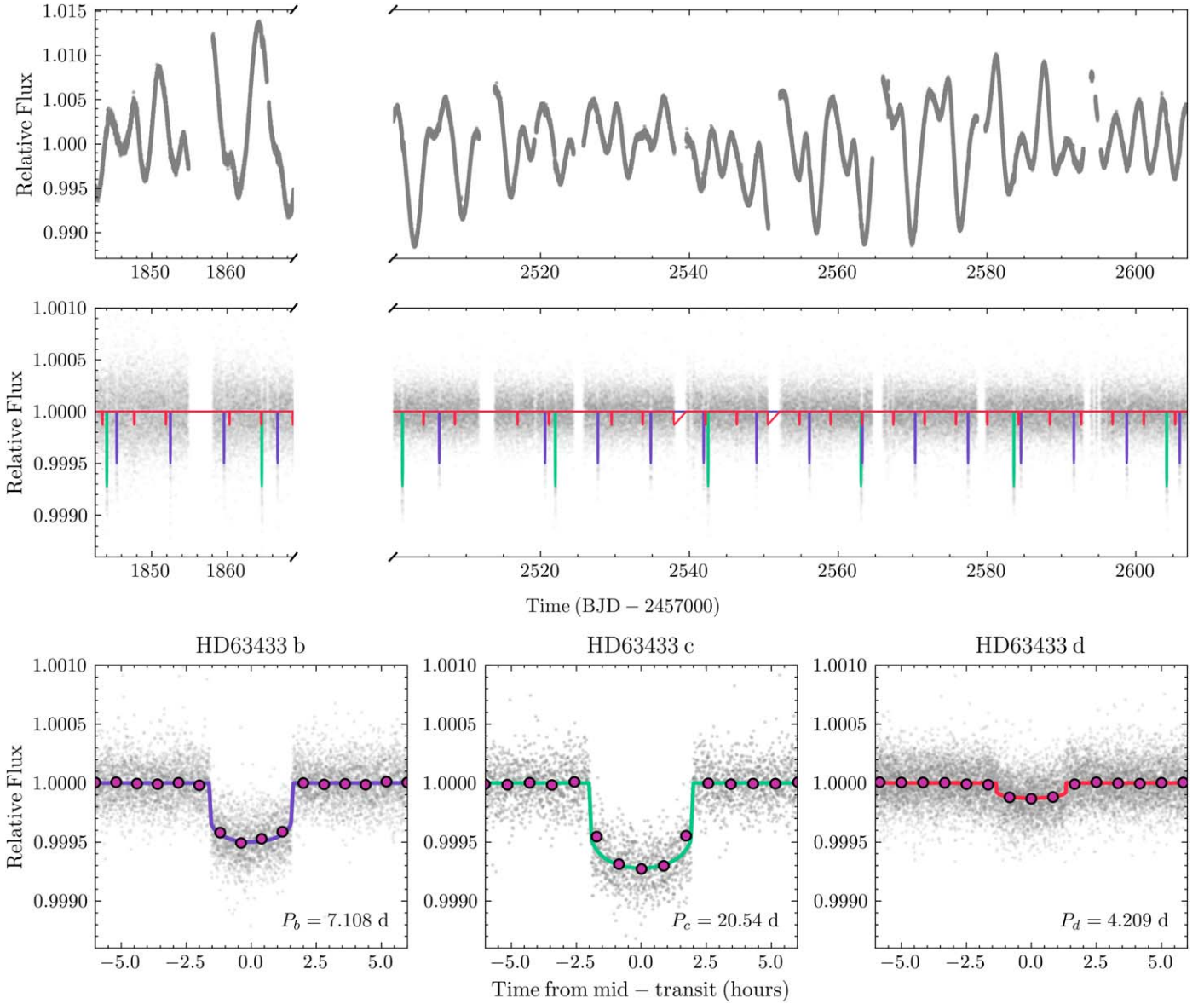
---

[40] https://github.com/adamkraus/Comove

Figure 1. The top panel shows the unflattened TESS light curve of HD 63433. The middle panel shows the flattened light curve with our three best-fit transit models for planets b, c, and d, as determined by our `edmcmc` outputs. The colors of these models correspond to each of the three planets as shown in the bottom panels, which depict the phase-folded light curves for each HD 63433 planet with binned data (red points) plotted over our best-fit models.

algorithm (Stellingwerf 1978); and an autocorrelation function (ACF; McQuillan et al. 2013).

These three period-search techniques were implemented on light curves from each individual sector, while the LS and PDM techniques were also implemented on a full light curve, comprised of all available sectors stitched together. The ACF technique was applied only to individual sectors because the large gaps between TESS observations adversely affected the results.

We searched for periodic signatures within a period range of 0.04 day (twice the integration time) to 30 days. If the observational baseline (τ) for a given source was less than 90 days, we reduced the maximum period-search limit to $\tau/3$. We performed a by-eye analysis of all resulting power spectra, autocorrelation plots, and phase-folded light curves corresponding to the strongest three periods of each of the periodograms. Two individuals from our collaboration team inspected the periodogram results for each candidate to search for signs of a periodic signature and determine the corresponding rotation

period. When discernible, the photometric rotation periods for a given source were cataloged along with an accompanying error estimate, which we estimated by taking the larger of either the error calculated by the PDM periodogram (Schwarzenberg-Czerny 1997) or 10% of the rotation period (to account for systematic uncertainties in the rotation period estimates).

In some cases, we observed that TESS instrumental systematics on the timescale of the spacecraft's orbit obscured very short-period rotation signals. To better recover the rotation periods in these cases, we then searched the light curves with all three methods (LS, PDM, and ACF) after high-pass-filtering the light curve by fitting a B-spline with break-points spaced every few days to the light curve and subtracting out the best fit and adding 1 (to return to the original normalization scale). We also introduced discontinuities in the B-spline at the beginning of each new TESS orbit to better model the rapid systematic changes in flux due to the scattered light from the spacecraft's close passage near Earth. Performing this additional analysis on

the high-pass-filtered light curve led to the identification of several additional rotators, mostly with very short rotation periods (less than 2 days).

We measure photometric rotation periods for 56 of the 130 stars, which we list in Table 6. We refer to these 56 sources as UMa members from this point forward. Aside from our planet host, which is presented in bold typeface in the top row, the sources are listed in ascending order by reddened-corrected color. In all cases, the reddening correction was less than 1% of the total BP–RP. The table also provides the TESS Input Catalog (TIC) ID, spatial coordinates, apparent and absolute Gaia magnitudes, apparent and absolute colors, distance from Earth, and RUWE value. Our cataloged UMa members are all bright, nearby targets, ranging between 12 and 57 pc from the Earth and 14.6–4.5 mag in apparent Gaia magnitude.

4.2.3. Rotation Sequence Consistency among UMa Members

The correlation between color and stellar rotation period (gyrochronological sequence) in moving groups has been well documented (e.g., Barnes 2007; Hartman et al. 2010; Douglas et al. 2016; van Saders et al. 2016). This relation builds upon the foundational work of Skumanich (1972), who discovered a correlation between the average rotational velocity ($v \sin i$) and the age of a given stellar cluster.

We illustrate the color–rotation sequence of our UMa catalog members in Figure 2. We annotate the top of the figure to indicate the range of spectral types, adding shaded panels that correspond to the hexadecimal color codes for a given spectral type (corresponding to luminosity class V and subclass 5), as reported by Harre & Heller (2021). The gyrochronological relation only holds for main-sequence stars, however; as we will show in Section 4.2.4, our UMa catalog members are all positioned along the main sequence. Therefore, we include the full UMa catalog in Figure 2. UMa catalog sources that are likely isolated (RUWE <1.2) are denoted as crimson circles, while potential binaries (RUWE ⩾1.2) are depicted as crimson squares (both contain error bars). UMa sources reported in Mann et al. (2020) but not included in our catalog are shown as light blue squares/circles (the same RUWE criterion applies here). We also plot members of the 670 Myr Praesepe cluster (Douglas et al. 2017) and the 120 Myr Pleiades cluster (Rebull et al. 2016), incorporating the Gaia DR3 reddening-corrected color to optimally align the three systems. In cases where the reddening corrections were not available (such as the small subset of Mann et al. 2020; UMa catalog sources not included in our catalog), we annotate symbols with an "x" symbol.

The UMa sources form a well-defined color–rotation sequence, with bluer, more massive UMa members exhibiting shorter periods. For redder UMa members, the rotation period increases for lower mass stars until the tight sequence ends for M-dwarf members, and the rotation periods are more randomly distributed. Importantly, our planet-hosting star, HD 63433, falls well within the UMa color–rotation sequence, corroborating its association with the moving group. It is shown in the plot as a gold star.

Our updated color–rotation sequence has several additional interesting features. We measure a rotation period of 0.77 day for the bluest UMa catalog source (F1V spectral type), which is well aligned with the rotation periods of F1V stars in other young clusters, including the two shown in Figure 2. The slope of the color–rotation relation and the corresponding point of divergence (the mass below which there is no tight rotation

sequence) are age-dependent, with older clusters exhibiting steeper slopes and divergences from the relation at lower masses. We observe that, for our UMa catalog members, the divergence from the color–rotation relation occurs for sources later than spectral type M1V, as would be expected for a cluster with an age estimate of 414 ± 23 Myr (Jones et al. 2015). In contrast, this divergence occurs at spectral type K4V for the younger Pleiades cluster and at later M-type for the older Praesepe cluster. UMa's color–rotation relation for FGK stars also shows a slope intermediate to that of the Pleiades and Praesepe systems, corroborating the fact that UMa's age is between that of those two clusters.

4.2.4. Color–Magnitude Diagram Consistency among UMa Members

We also assessed whether HD 63433's color–magnitude diagram position is consistent with that of the other UMa catalog members. We find that our UMa catalog members are well-matched to a 400 Myr, [M/H] = 0.02 dex stellar isochrone, as shown by the result drawn from the PARSEC (version 1.2S) in Figure 3 (Bressan et al. 2012).[41] We find that HD 63433 (shown as a gold star in Figure 3) falls precisely in the sequence of other UMa members in color–magnitude space, in close agreement with the PARSEC isochrone prediction, as expected for a single star member of the group.

The fact that the UMa candidate members closely match a 400 Myr isochrone is encouraging for the fidelity of the sample, and suggestive that the stars are coeval, but because of the spectral types of our candidate members, this is not a particularly stringent test. As described in Section 1, the color–magnitude diagram (CMD) location of GKM main-sequence stars is consistent with that for isochrones spanning several billion years; therefore, only sources with strong departures from the isochrone can be flagged as potential field candidates. Such departures may arise among main-sequence stars with appreciably different metallicity but also may arise from binarity and/or nonstandard stellar evolution.

We do see some such deviations from the color–magnitude sequence for a handful of candidate UMa members in Figure 3. In particular, a handful of sources included in the Mann et al. (2020) analysis, but excluded from our list of candidate members (shown as blue circles/squares), show significant departures from the CMD. We attribute these deviations from the color–magnitude sequence to the effects of binarity, where the combined light from blended binary stars causes the unresolved source to sit above the color–magnitude sequence in absolute magnitude. Supporting the binary hypothesis is the fact that 4/5 of these stars were excluded from our sample because of their high RUWE metrics (RUWE > 2).

We note that other possible causes for deviations from a tight color–magnitude sequence include a range of spot filling factors (that are not included in models) or incorrect or missing corrections for extinction and reddening. We suspect the former explanation is more likely because reddening corrections are negligible for UMa members due to their proximity. The average line-of-sight reddening correction (E(BP-RP)E(BP–RP)) for our UMa catalog sources is 0.002 ± 0.001 mag, much less than the uncertainties on these quantities. We label the sources missing these corrections with an "x" symbol.

We annotate the top of Figure 3 to indicate the range of spectral types included on the color–magnitude diagram,

---

[41] http://stev.oapd.inaf.it/cgi-bin/cmd

Table 6
Properties of the 56 Likely Members of UMaG Included in Our Catalog (Listed in Ascending Order by Reddened-corrected Color, `BP-RP_abs`)

TIC ID	R.A. (deg)	Decl. (deg)	Gmag (mag)	Gmag_abs[a] (mag)	BP–RP (mag)	BP-RP_abs[b] (mag)	Dist (pc)	RUWE	Prot (d)	e_Prot (d)
130181866	**117.479**	**27.363**	**6.737**	**4.988**	**0.854**	**0.854**	**22.34**	**0.99**	**6.4**	**0.6**
235682463	287.2912	76.5605	5.032	2.846	0.445	0.445	27.46	1.10	0.77	0.1
86433449	214.8178	13.0043	5.289	3.205	0.549	0.549	26.09	1.10	1.5	0.2
408908804	92.0267	−15.9012	6.843	3.516	0.597	0.597	46.23	0.93	1.7	0.2
362747897	247.1172	−70.0844	4.744	4.336	0.737	0.737	12.04	2.11	8.2	0.8
283792884	63.8700	6.1869	6.175	4.456	0.743	0.743	22.05	1.10	6.5	0.7
157272202	198.4042	56.7083	6.663	4.659	0.780	0.780	25.12	1.00	6.0	0.6
329574145	271.5988	−36.0198	5.805	4.638	0.781	0.781	17.10	0.55	6.0	0.6
417762326	129.7988	65.0209	5.499	4.701	0.804	0.804	14.45	1.17	4.9	0.5
24910401	27.3473	−10.7036	6.590	4.695	0.808	0.808	23.21	7.40	8.7	0.9
283792891	63.8574	6.1997	6.778	5.059	0.860	0.860	22.05	1.05	6.5	0.7
88659764	152.5783	38.4135	8.685	5.013	0.864	0.863	53.89	1.08	7.3	0.7
117881543	96.8361	−33.1140	8.228	5.002	0.865	0.865	44.12	1.12	7.3	0.7
366351891	125.7439	7.6304	8.990	5.458	0.954	0.954	50.77	0.89	5.2	0.5
366351890	125.7473	7.6309	9.031	5.495	0.959	0.957	50.41	0.93	5.2	0.5
415563103	91.6687	15.5421	6.539	5.550	0.984	0.984	15.76	0.98	8.1	0.8
176471832	86.9683	−2.7606	9.104	5.693	1.015	1.009	47.45	0.97	8.2	0.8
16045498	113.2524	37.0298	7.426	5.848	1.057	1.057	20.65	1.03	8.0	0.8
149852612	44.6862	40.0723	9.559	6.152	1.081	1.081	47.94	1.21	9.5	1.0
308056339	99.4094	16.2704	9.670	6.064	1.104	1.104	52.54	1.17	15.2	1.5
288158059	98.2995	−17.4905	8.909	6.126	1.120	1.119	36.05	1.11	9.0	1.0
99381773	190.4355	55.7247	7.985	6.203	1.156	1.156	22.69	0.97	12.0	1.2
224305606	188.9637	51.2215	8.258	6.167	1.169	1.169	26.18	1.31	9.0	1.0
105577896	153.3202	42.3554	10.494	6.710	1.298	1.298	56.98	1.09	9.6	1.0
198381449	257.5438	54.4944	8.475	6.839	1.397	1.397	21.23	0.97	11.6	1.2
419366667	121.0079	−35.2761	10.388	7.077	1.489	1.444	44.73	2.89	11.7	1.2
198381445	257.5515	54.4901	8.851	7.214	1.534	1.534	21.21	0.97	11.6	1.2
97526849	167.4684	21.6255	10.508	7.468	1.634	1.634	40.46	1.04	12.7	1.3
95618424	121.4938	26.2814	9.475	8.158	1.903	1.902	18.34	1.14	13.6	1.4
176469654	86.8249	−0.0136	10.207	8.134	1.914	1.912	25.83	1.05	15.0	1.5
97488127	165.6598	21.9671	8.811	8.426	2.006	2.005	11.92	1.12	13.6	1.4
464452462	282.6110	−62.0510	9.883	8.765	2.087	2.087	16.76	0.97	8.0	0.8
159503663	246.4935	83.4067	11.028	8.722	2.121	2.119	28.88	1.16	16.7	1.7
139053298	182.2063	30.3503	11.481	9.223	2.272	2.272	28.13	1.05	8.6	0.9
386955374	172.8537	13.7454	11.844	9.049	2.289	2.289	36.27	0.97	4.5	0.5
390733970	44.0827	61.6896	12.289	9.592	2.369	2.369	34.72	1.13	4.5	0.2
290970527	309.0346	−36.1199	10.587	9.449	2.395	2.395	16.89	1.17	2.1	0.2
165599288	227.2838	59.0738	11.884	9.545	2.439	2.437	29.18	1.34	4.0	0.4
98506634	227.6127	13.4671	12.545	10.260	2.642	2.642	28.58	1.30	1.8	0.2
77896213	78.8634	−35.8070	13.062	10.437	2.649	2.646	33.33	1.23	10.6	1.0
20118579	130.1653	45.0045	13.578	10.418	2.709	2.709	42.79	1.26	7.3	0.7
313110473	211.0967	72.4130	13.115	10.452	2.740	2.740	33.99	1.27	4.9	0.5
290474796	139.0424	1.8858	11.689	10.716	2.764	2.764	15.64	1.12	1.5	0.2
309661100	116.8078	50.3440	11.782	11.035	2.799	2.799	14.11	1.41	0.77	0.1
219463771	208.4116	77.6189	11.540	10.929	2.803	2.803	13.25	1.20	1.25	0.1
291962446	106.2752	4.3343	14.581	11.144	2.825	2.824	48.60	1.08	0.75	0.8
80949873	122.0214	59.6077	13.498	10.916	2.839	2.834	32.59	1.23	2.7	0.3
72882364	86.1131	−4.1004	13.247	11.365	2.866	2.866	23.82	1.17	0.9	0.1
72636078	218.0450	16.0137	12.241	11.251	2.867	2.867	15.71	1.36	0.77	0.1
162131472	249.4300	−20.2261	12.326	10.856	2.872	2.872	19.68	1.30	3.4	0.4
61627029	78.3220	27.6173	13.765	11.126	2.941	2.898	32.70	1.12	1.4	0.1
219787770	264.5203	65.1575	13.575	10.764	2.942	2.898	35.44	1.29	0.4	0.1
396948416	179.6839	10.3325	14.431	11.299	2.955	2.953	42.23	1.23	0.9	0.1
21220201	128.9103	16.4825	14.346	11.744	2.983	2.983	32.92	1.16	0.2	0.1
17992446	171.0182	38.1364	13.008	11.677	3.017	3.017	18.43	1.41	0.5	0.1
141821609	206.2412	55.4728	13.930	11.846	3.025	3.025	26.02	1.33	0.3	0.1

Notes. While the rotation periods and errors (`Prot` and `e_Prot`) were determined by this work, all other properties were obtained from Gaia DR3. We show the properties of HD 63433 in the top, bold row. Comments about individual catalog sources are not included here, but are available in the digital version of the catalog.
[a] The absolute Gaia magnitude, such that $G_{abs} = G + 5 \times \log_{10}(\varpi/100) - A_G$.
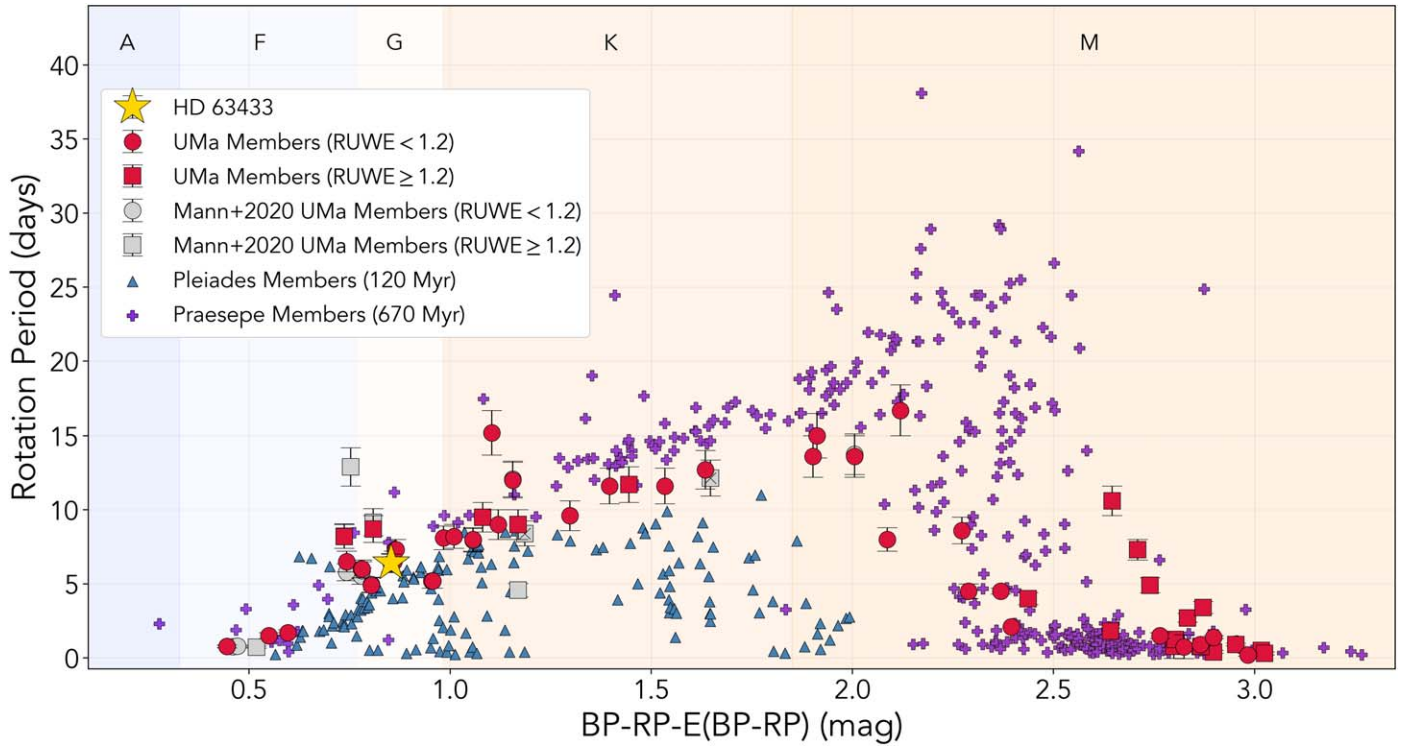[b] The absolute BP–RP color, such that BP-RP_abs=BP-RP-E(BP-RP).

Figure 2. The color–rotation sequence for catalog members of the UMa moving group, as compared to the 120 Myr Pleiades (Rebull et al. 2016) cluster and the 670 Myr Praesepe cluster (Douglas et al. 2017). Circles indicate UMa sources with RUWE <1.2, while squares indicate those with RUWE ⩾1.2. Our target HD 63433 is shown as a gold star. Light blue circles/squares denote UMa sources featured in Mann et al. (2020)—those shown with an "x" symbol overplotted lack Gaia DR3 reddening values required for absolute calibration. We identify the spectral types investigated, adding shaded panels that correspond to the hexadecimal color codes for a given spectral type (luminosity class V, subclass 5), as reported by Harre & Heller (2021).

adding shaded panels that correspond to the hexadecimal color codes for a given spectral type (luminosity class V, subclass 5), as reported by Harre & Heller (2021). Our UMa catalog members range in spectral type between F1V and M5V, which corresponds to a mass range of 1.6–0.2 $M_\odot$ (as determined by a fit to the PARSEC isochrone).

For the sake of completeness and to include more evolved/luminous stellar members in this catalog, we searched for kinematic matches among subclass IV targets and main-sequence stars of earlier spectral types that were included in prior UMa catalogs (before the kinematic precision made available by the Gaia mission), drawing from resources such as Miczaika (1948), Soderblom et al. (1993). Such sources could help to establish a more well-defined main-sequence turnoff point, which would permit the calculation of a main-sequence turnoff mass and corresponding age for the UMa system. However, we were unable to identify any kinematic matches. Part of the difficulty in our search for more luminous kinematic members is because Gaia DR3 radial velocity measurements were often not available for these sources. A targeted radial velocity follow-up study would offer the potential to identify more luminous kinematic UMa members.

4.2.5. Lithium Sequence Consistency among UMa Members

The abundance of lithium in the stellar photosphere is another important age diagnostic for young stars (Jeffries 2014; Barrado 2016). Therefore, we searched the literature for measurements of the lithium abundance for our UMa members. We computed a weighted average of the lithium values found in the literature (from the sources described in Section 2.7). In Figure 4, these results are illustrated as a function of reddening-corrected color. To provide a consistent contrast, we illustrate the color–A(Li) relations for members of the Pleiades and Praesepe clusters (Cummings et al. 2017; Bouvier et al. 2018). For the Pleiades and Praesepe members depicted, effective temperatures were transformed to reddening-corrected colors using the color conversion function described in Mucciarelli et al. (2021).

We found that roughly 20% of our UMa catalog sources have published lithium abundance measurements. These sources form a clear color–lithium sequence, and the large A(Li) measurements are reflective of a young stellar association. Once again, the lithium abundance for HD 63433 (shown as a gold star) falls well within the sequence of the other UMa group candidate members, strengthening the case for its association with the group. Similar to the color–rotation sequence, UMa's color–lithium relation is shown to map out a region intermediate to that of the Pleiades and Praesepe systems, corroborating the fact that UMa's age is between that of those two clusters.

In Figure 4, we include a dashed horizontal line indicating the solar system meteoritic lithium abundance value of 3.3 dex (Asplund et al. 2009). This is the value corresponding to the initial lithium supply of a given star before the onset of depletion. We also note evidence for a lithium dip feature, known to impact A- and F-type stars (Boesgaard & Tripicco 1986). The departure from a monotonic relation between lithium abundance and color is seen for stars earlier than F5V spectral type, which corresponds to stars with effective temperatures ⩾6600 K. Our bluest UMa catalog source (F4V spectral type) is shown to coincide with the center of the lithium dip feature, strongly departing from the nearly

Figure 3. Color–magnitude diagram of HD 63433 (gold star) and our catalog of UMa comoving members (crimson circles/squares). Same legend definitions as Figure 2. In black, we illustrate a PAdova and TRieste Stellar Evolution Code (PARSEC) isochrone (version 1.2S) for a 400 Myr system with [M/H] = 0.02 dex (Bressan et al. 2012). We identify the spectral types investigated, adding shaded panels that correspond to the hexadecimal color codes for a given spectral type (luminosity class V, subclass 5), as reported by Harre & Heller (2021).

Figure 4. Color–A(Li) sequence of our cataloged UMa members (crimson circles/squares) with HD 63433 depicted as a gold star. Same legend definitions as Figure 2. Twelve sources in our catalog had published A(Li) abundances. The solar system meteoritic abundance level of 3.3 dex is depicted as a horizontal dashed line (Asplund et al. 2009). To indicate the range in stellar types, we illustrate the hexadecimal color codes reported by Harre & Heller (2021; luminosity class V, subclass 5). The color–A(Li) relation for the 120 Myr Pleiades cluster (Bouvier et al. 2018) and the 670 Myr Praesepe cluster (Cummings et al. 2017) are shown as a comparison. A/F-type stars in all three systems show evidence of the well-known lithium dip feature (Boesgaard & Tripicco 1986).

monotonic color–A(Li) relation traced out by the other UMa catalog sources.

Our updated view of this larger population of UMa members does not change the original conclusion that HD 63433's properties are highly consistent with the group's constituent stars. We, therefore, consider HD 63433 to be a member of UMa, and apply the group's age measurement of 414 ± 23 to HD 63433 and its planetary companions (Jones et al. 2015).

5. Ruling out False-positive Scenarios

5.1. Possible False-positive Scenarios

Sometimes, scenarios other than transiting exoplanets can cause apparent dips in the brightness of stars, so transiting exoplanet detections, like that of HD 63433 d, require scrutiny and analysis before they can be considered solid. One way to increase confidence in exoplanet detections is called *confirmation*, which involves detecting the signal of the planet with an independent detection method. Confirmation often requires expensive follow-up observations, and in many cases is

unfeasible given the sensitivity of other detection techniques. Another way to increase confidence in exoplanet detections is "validation," which involves quantifying, testing, and rejecting all other possible false-positive scenarios (such as eclipsing binary, blended binary, stellar spots, or instrumental artifacts; see Ciardi et al. 2015), leaving a real exoplanet as the most probable explanation for the candidate transit signal. Because confirmation of HD 63433 d is likely beyond the capabilities of current precise radial velocity observations (because of HD 63433's high-amplitude stellar variability), we use the validation approach to show that HD 63433 is overwhelmingly likely to be a real exoplanet.

In particular, we address the following classes of false-positive signals and show that HD 63433 d cannot be caused by each scenario:

1. *Signal arises from instrumental effects and/or stellar variability.* One possibility is that the detected signal is an instrumental artifact or a false alarm resulting from high-amplitude stellar variability. Typically, in such cases, we would anticipate variations in the signal's shape, amplitude, and other attributes across different sections of the light curve. This is because instrumental glitches or stellar variability features are not expected to repeat in perfectly periodic intervals, corresponding to a 4.2 days orbital

period. We test this scenario for HD 63433 d by assessing the consistency of the transit signal between different transits and different sectors. We found no evidence for variable transit depths. The signal's period is distinct from the stellar rotation period and its harmonics, and there are no known TESS instrumental systematics that repeats every 4.2 days. We also confirmed visually that no anomalies in the background flux took place at the times of the transits of HD 63433 d in any of the observed sectors. We conclude that the signal is astrophysical and caused by an orbiting object.

2. *HD 63433 itself is an eclipsing binary.* Some stellar eclipses (especially grazing eclipses of small stars) are difficult to distinguish from planetary transits without additional observations, which can be a source of false positives among a list of planetary candidates. It is straightforward to rule this scenario out by collecting radial velocity observations of the host star, as stellar-mass companions will cause Doppler shifts with amplitudes much greater than $1 \mathrm{~km~s}^{-1}$. Dozens of radial velocity observations collected over the years, and described in Section 2.2, show no velocity shifts greater than about $100 \mathrm{~m~s}^{-1}$. Given that the predicted radial velocity semiamplitude (K) values corresponding to an equal mass binary system and a G-type + M-type binary system are much larger than these measurements (8×10^4 and $5 \times 10^4 \mathrm{~m~s}^{-1}$, respectively), HD 63433 itself cannot be an eclipsing binary.

3. *Contamination by eclipsing binaries.* TESS has a focus-limited PSF with a large pixel scale of approximately $21''$, so the photometric masks used to extract light curves are large and include flux from several other nearby stars. Thus, these nearby stars that are unresolved by TESS but can be resolved by ground-based telescopes can sometimes introduce contaminating signals that mimic planetary transits. For context, the number of known Gaia sources (including HD 63433) within the TESS photometric apertures are 10 sources in Sector 20, 9 sources in Sectors 44 and 45, 8 sources in Sector 46, and 12 sources in Sector 47. Using the seeing-limited ground-based observations described in Sections 2.3 and 2.4, we placed an upper limit of $6''6$ on the radius of confusion regarding this possibility. Our observations from the LCO telescope at McDonald Observatory and the archival ZTF light curves we created with DEATHSTAR place a tight upper limit on the radius of confusion among eclipsing binaries with HD 63433 d's orbital period.

In addition to nearby eclipsing binaries far enough from HD 63433 to be resolved by seeing-limited ground-based telescopes, sometimes false positives are caused by eclipsing binaries close enough to be blended with the target in ground-based images. The vast majority of these targets can be ruled out by adaptive optics observations, which can increase the resolution of ground-based telescopes by orders of magnitude and reveal faint stars that could be the source of the transits.

We quantified how bright any given star must be to cause the transits we observe for HD 63433 d. Following Vanderburg et al. (2019), we fit the light curve again with MCMC to measure the duration of transit ingress and egress for this new signal, while imposing no physical constraints (e.g., not requiring Kepler's third law be

obeyed). We converted this ingress/egress duration into an effective magnitude limit and found that with 99.7% confidence, for a blended star to mimic HD 63433's transit signal, it must be within 5.57 mag of the target star's brightness. The existing adaptive optics imaging rules out stars this bright at distances greater than about 150 mas from the target.

With just a single adaptive optics observation, it is still possible (although very unlikely) that an eclipsing binary could reside at the precise location of the star. This false-positive scenario can be ruled out with multiple adaptive optics observations over a large temporal baseline. Over the nearly 17 yr between the first deep archival adaptive optics observation of HD 63433 (as described in Ammler-von Eiff et al. 2016) and our new observations reported in this paper, the star's apparent position has moved by over 250 mas due to its proper motion. Both the archival adaptive optics observation taken in 2004 and our new Keck observation have a sensitivity to companions with contrast greater than 5.57 mag at 250 mas separations (at near-infrared wavelengths, so even greater contrast at visible wavelengths where TESS observes). Therefore, combining these adaptive optics observations makes it possible to rule out all background eclipsing binaries bright enough to cause the transit signal of HD 63433 d.

4. *Physically associated eclipsing binaries.* One final false-positive scenario is that a physically associated (comoving) faint companion star to HD 63433 is an eclipsing binary. This cannot be completely ruled out with multiple adaptive optics observations over time, because the companion moves with the target and could remain so close to being blended even in the high-resolution observations. However, to remain undetected by our high-angular-resolution observations, an eclipsing binary companion would have to orbit at a distance less than about 3 au, and therefore with orbital periods less than about 5 yr. Such a stellar companion would be easily detected in the archival RV observations if it exists, except in extremely finely tuned and unlikely (probability less than 10^{-4}) face-on inclinations that would reduce the RV shifts to less than about $100 \mathrm{~m~s}^{-1}$. Therefore, with high confidence, we conclude that there are no physically associated eclipsing binaries that could mimic the signal of HD 63433 d.

Since we can confidently rule out all of these possible false-positive scenarios, we conclude that the overwhelmingly likeliest explanation for the observed transit signal is that HD 63433 d is a genuine exoplanet and consider it validated.

5.2. Statistical Validation with TRICERATOPS

To double-check our conclusion that no false-positive scenarios can mimic the signal of HD 63433 d, we employed the TRICERATOPS pipeline (Giacalone et al. 2021) to calculate the likelihood of false-positive scenarios. TRICERA-TOPS computes the probability that an input light curve originates from a wide range of scenarios using Bayesian inference. The pipeline takes into account several astrophysical false-positive configurations, including those discussed above, and calculates the false-positive probability (FPP), which is the probability that the observed transit is not caused by a planet
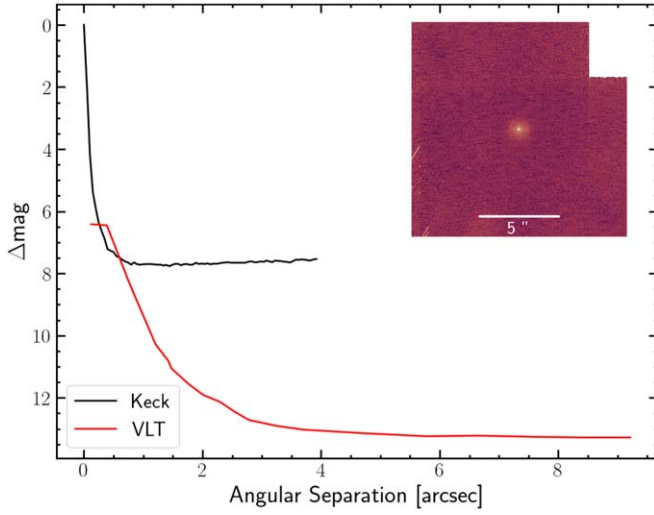
Figure 5. Contrast curves obtained from Keck/NIRC2 high-contrast observations (black line; Br-γ filter) and VLT observations (red line; K filter). The 5σ contrast limits for secondary sources are plotted against angular separation.

(e.g., an eclipsing binary) and the nearby false-positive probability (NFPP), which is the probability that the signal comes from a nearby resolved star. A planet is considered statistically validated when the false-positive scenarios can be ruled out with a certain level of confidence, typically the FPP <0.01 and the NFPP <0.001 (Morton 2012, 2015; Rowe et al. 2014; Giacalone et al. 2021). We ran TRICERATOPS using the light curve for planet d, with the transit signals for planets b and c removed, phase-folded on the period from our edmcmc models. Furthermore, we also implemented the Keck NIRC2 high-contrast imaging AO observations described in Section 2.5 as well as observations from the Very Large Telescope (VLT) reported in Ammler-von Eiff et al. (2016), to better constrain the overall calculation. The contrast curves corresponding to these two observations are shown in Figure 5. We obtained FPP $=(1.1 \pm 2.5) \times 10^{-5}$, and NFPP $= 0$ for the signal associated with HD 63433 d. This value for FPP falls well below the customary threshold of 10^{-3} for a statistically validated planet and agrees with the claims discussed in Section 5.

6. Discussion

6.1. Physical Parameters of HD 63433 d

Based on the results of our analysis, HD 63433 d can be described as a *hot Earth*. Our MCMC modeling, combined with derived stellar parameters, yields a radius of $1.073^{+0.046}_{-0.044}\ R_\oplus$, just slightly larger than the size of our home planet. The planet orbits HD 63433 every $4.209075^{+0.000012}_{-0.000023}$ days (these errors are on the order of 1 s). The planet has a semimajor axis that is about 20 times smaller than that of Earth ($0.0503^{+0.0025}_{-0.0027}$ au). We constrain the eccentricity to be moderate at most (<0.52 at 84% confidence, and <0.73 at 95% confidence), but our posterior draws are consistent with a perfectly circular orbit. This would be in line with results from Kepler for planets in multitransiting systems (Van Eylen et al. 2019).

The orbital period ratios of planets b and d are close to resonance. However, since the ratio is slightly interior to the location of the resonance, it is unlikely that the system is in resonance, as the pile-up of resonant systems occurs slightly exterior to the resonance (Fabrycky et al. 2012).

The equilibrium temperature, $T_{\rm eq}$, of HD 63433 d can be calculated assuming a circular orbit, an albedo (α) of 0.3, and perfect heat redistribution, such that

$$T_{\rm eq} = T_{\rm eff}(1 - \alpha)^{1/4}\sqrt{\frac{R_\star}{2a}}, \qquad (4)$$

where a is the planet's semimajor axis, $T_{\rm eff}$ is the stellar effective temperature, and $R_\star$ is the radius of the host star. Leveraging the values provided in this paper, this results in an equilibrium temperature of $T_{\rm eq} = 1040 \pm 40$ K.

However, radial velocity observations (e.g., Rogers 2015) have shown that planets the size of HD 63433 d almost always have predominantly rocky compositions and no thick atmospheres (although note that these observations come almost exclusively from stars older than HD 63433; see Section 6.3). If HD 63433 d is indeed predominantly rocky, then it likely has no thick atmosphere that could efficiently redistribute heat, as assumed by Equation (4). Therefore, we estimate the dayside temperature of HD 63433 d under the assumption of a tidally locked blackbody (i.e., a rocky surface with no atmosphere). The assumption that the planet is tidally locked is supported by the tidal locking timescale, as calculated from Gladman et al. (1996). More specifically, assuming a tidal Q of 100 and an initial rotation rate of one cycle per day, we derive a tidal locking timescale of $t_{\rm loc} \approx 10^3$–10^4 yr, which is much shorter than the age of the system. According to Cowan & Agol (2011), the apparent observed dayside temperature ($T_{\rm day}$) of a planet in a noneccentric orbit, with no heat redistribution to its night side,[42] can be expressed as

$$T_{\rm day} = [2/3(1 - \alpha)]^{1/4}T_{\rm sub}, \qquad (5)$$

where $T_{\rm sub} = T_{\rm eff}(R_\star/a)^{1/2}$ and represents the temperature at the planet's substellar point (the point on the planet's surface such that the host star is at the zenith). Assuming $\alpha = 0$ (similar to the measured albedo for the rocky planet Trappist-1b; Greene et al. 2023), we calculate that the dayside temperature of HD 63433 d is approximately $T_{\rm day}=1530$ K ($a = 0.0481$ au). The planetary temperature resembles other lava planets, such as CoRoT-7b and Kepler-10b (Léger et al. 2009; Batalha et al. 2011).

6.2. HD 63433 d in Context

HD 63433d's small size and precisely known young age, in combination with the proximity and brightness of its host star, make it stand out from the known population of exoplanets in several ways. First, HD 63433 d is the smallest known planet with a precisely measured age that is less than 500 Myr, making it an important touchstone for understanding how Earth-sized planets evolve. This is shown in Figure 6, which depicts the planet radius as a function of the orbital period for all confirmed exoplanets (NASA Exoplanet Archive, Akeson et al. 2013). While the full sample is shown in gray, we highlight in blue the relatively small subset of planets with precisely measured ages less than 500 Myr. For context, we considered a system age estimate to be precisely measured if its error estimate is at most 50% of the estimated age value. Note that the apparent lack of planets older than 500 Myr with orbital periods greater than 10^4 days is because the technique used to

---

[42] At a constant albedo, the planet's dayside temperature is greater than the equilibrium temperature by a factor of $\approx$1.28.
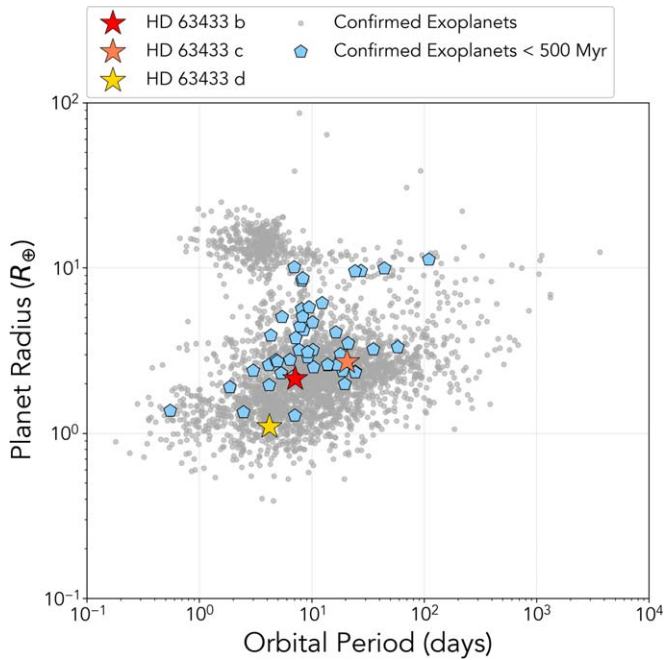
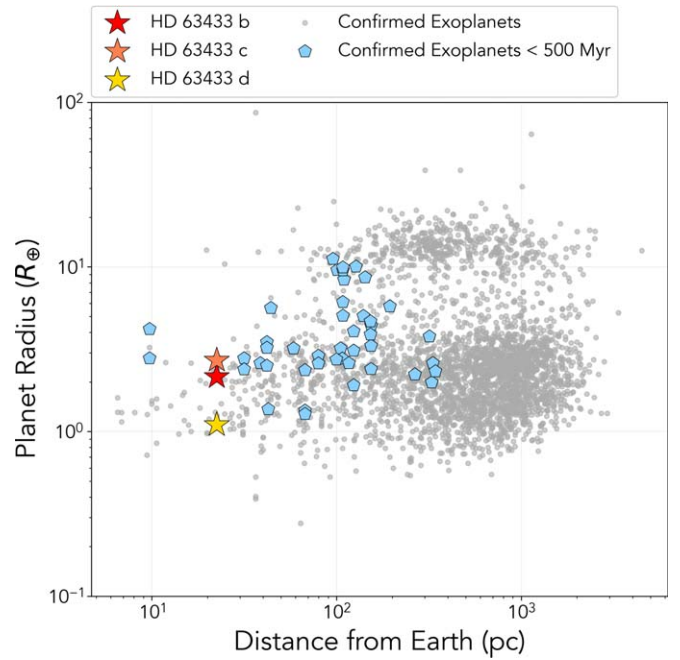**Figure 6.** Planet radius vs. orbital period for confirmed exoplanets (gray circles), confirmed exoplanets with reliable age estimates that are <500 Myr (blue pentagons), and the three HD 63433 planets (b, red star; c, orange star; and d, yellow star). Note that there are few detections of young, Earth-sized planets. Those detected are in short-period orbits about their stellar hosts. For enhanced readability of the figure, we omit exoplanets detected via the direct imaging method, as their orbital separations are much larger.

Figure 7. Distance from Earth vs. planet radius for confirmed exoplanets (gray circles), confirmed exoplanets with reliable age estimates that are <500 Myr (blue pentagons), and the three HD 63433 planets (b, red star; c, orange star; and d, yellow star). Note that HD 63433 d is the nearest, young, Earth-sized exoplanet discovered to date.

find these objects (direct imaging) is biased toward young, bright systems.

HD 63433 is one of the nearest and brightest transiting planet hosts in the sky. According to the NASA Exoplanet Archive (accessed 2023 November 9), only seven transiting planet hosts[43] with brighter magnitudes in the TESS bandpass are known. None of these stars are particularly young or are members of clusters or associations. Therefore, HD 63433 is the brightest known host of young transiting exoplanets in the sky. The high rate of stellar photons from HD 63433 striking TESS's detectors enabled a high enough light-curve precision to detect the very shallow (100 ppm) transits of this Earth-sized planet.

HD 63433's brightness is due to its proximity (22 pc) to the solar system. Figure 7 depicts the population of confirmed exoplanets as a function of planet radius and distance from Earth to the host star. Among young stars hosting transiting planets, only AU Mic lies closer to Earth than HD 63433. HD 63433's close distance to Earth allows studies of atmospheric escape. Zhang et al. (2022) searched for signatures of ongoing photoevaporation in the two previously known planets, and observed Lyman α absorption from HD 63433 c, but not from HD 63433 b. Using hydrodynamical simulations, they showed that, if HD 63433 b had a H/He atmosphere, its photoevaporative outflow would have been observable. Those results suggest that HD 63433 b lost its primordial H/He atmosphere. HD 63433 d experiences a stellar flux twice as large as that of HD 63433 b; therefore, unless HD 63433 d is much more massive than standard mass–radius relations (e.g., Chen & Kipping 2016) predict, it likely lost its primordial H/He

atmosphere too. Observations and models similar to those of Zhang et al. (2022) could test this expectation and help understand the atmospheric evolution of the planet.

6.3. HD 63433 d: A Case Study for Atmospheric Loss

Currently, one of the most important inquiries in exoplanet science is understanding in which circumstances planets keep or lose their thick primordial hydrogen/helium atmospheres, and what physical processes drive this phenomenon. Population-level studies have revealed the presence of a gap in the radius distribution of small planets (Owen & Wu 2013; Fulton et al. 2017; Van Eylen et al. 2018; Zeng et al. 2019). Two of the leading mechanisms for understanding the formation of this feature, extreme ultraviolet photoevaporation (Owen & Wu 2017) and core-powered mass loss (Gupta & Schlichting 2019) differ most significantly in timescales on which they act, so a promising way to distinguish these mechanisms is to study atmospheric escape and mass loss for planets with known ages. Recent studies (Kreidberg et al. 2019; Crossfield et al. 2022; Greene et al. 2023; Zieba et al. 2023) have found that atmospheric loss is an important process for older terrestrial planets orbiting M-type stars. Given its radius well below the gap, HD 63433 d might be expected to have a rocky composition based on comparison with older planets, but if mass loss takes longer than $\approx$500 Myr, it might still have a thick envelope. Because Earth-sized planets orbiting young, Sun-like stars have so far been difficult to detect, HD 63433 d presents a particularly compelling case study for atmospheric investigations of close-orbiting Earth-sized planets.

6.4. Future Work Characterizing HD 63433

HD 63433 d presents intriguing and unique opportunities for future follow-up observations. It would be valuable to

---

[43] In order of ascending brightness: WASP 189, HR 858, HD 158259, 55 Cnc, pi Men, ν^2 Lup, and HD 219134.

interrogate the planet's mass using precise radial velocities and determine whether the composition is indeed rocky, as expected based on observations of older planets. However, this will be challenging due to the high-amplitude stellar radial-velocity variability, which has limited attempts to measure the masses of the larger HD 63433 planets (Damasso et al. 2023; Mallorquín et al. 2023). Due to its proximity to Earth and high temperature, it may be feasible to utilize the James Webb Space Telescope (JWST) to detect the thermal emission from HD 63433 d. Several JWST MIRI programs have been designed to capture the thermal emission of rocky exoplanets, but HD 63433 d is younger than all terrestrial worlds with planned JWST emission observations. Although HD 63433 d is more luminous than many planets targeted for MIRI thermal emission observations, we estimate that the planet's eclipse depth in the mid-IR will only be approximately 20–30 ppm due to its orbit around a relatively large, Sun-like star. MIRI should be capable of detecting such shallow eclipse depths; Bouwman et al. (2023) report 15 ppm bandpass averaged precision in commissioning data, so the systematic noise floor should not be an issue. Moreover, the star's unusual brightness should provide plenty of photons to make these sensitive measurements. Kempton et al. (2018) presented an emission spectroscopy metric (ESM) for terrestrial planets that is proportional to the expected S/N of a JWST secondary eclipse detection at the center of the MIRI LRS bandpass, a wavelength of 7.5 μm. For HD 63433 d, we calculate an ESM of 7.1 ± 0.3, comparable to what the authors of that study found for planet GJ 1132b, which they used as their benchmark for a small rocky planet orbiting a nearby, bright M-dwarf. The precisely known age of this planet makes secondary eclipse observations particularly interesting for probing the presence of an atmosphere.

Finally, TESS is scheduled to obtain another sector of observations of HD 63433 between 2023 November and December (Sector 72), and may continue observing the star in future mission extensions. These additional observations will improve the precision of parameters for the known planets and may reveal additional transit signals. In the Kepler catalog, among the 277 systems with at least three transiting planet candidates, 35% (98 total) host at least one additional planet. Although we find no additional transit signals in the BLS and TLS searches after removal of the three transit signatures, the odds of HD 63433 itself hosting additional planets that may be revealed with additional observations are not insignificant.

6.5. Future Work Characterizing the Ursa Major Moving Group

An important result of our work is that we have identified many new members of the Ursa Major moving group using new radial velocity measurements from Gaia DR3. We identified a set of 56 likely members based on kinematics and photometric rotation period analysis, which allowed us to significantly increase the number of Ursa Major sources with measured rotation periods and show a coherent rotation sequence with an age intermediate to that of the Pleiades and Praesepe clusters. The new observations from Gaia DR3 promise significant further improvements to the membership and properties of the moving group. We excluded many stars from further analysis based on the lack of radial velocity measurements from Gaia DR3. Since Gaia RVs are only measured with short exposures in the region of the Ca infrared triplet lines, hot stars with a few broad lines are likely systematically excluded. Ground-based follow-up may reveal that some of the sources we excluded, especially hot stars, indeed appear to be kinematic cluster members. Identifying new hot/massive stellar members could yield better constraints on the group's age through color–magnitude diagram fitting. It may even be possible to measure asteroseismic oscillations for any members that exhibit pulsational signatures. Moreover, ground-based spectroscopic follow-up of potential UMa members to measure lithium abundances will provide another important constraint on the group's age. Future characterization of the Ursa Major group itself will ultimately enhance our knowledge of the HD 63433 multiplanet system.

7. Summary

In this work, we have presented the discovery and characterization of an Earth-sized planet orbiting the nearby, bright young star HD 63433. This is the third planet to be detected in the HD 63433 system. The system is a likely member of the UMa moving group. We analyzed TESS data to study the planet candidate and analyzed the properties of the UMa moving group to assess its membership.

HD 63433 d is an Earth-sized ($1.073^{+0.046}_{-0.044} R_\oplus$) planet orbiting a nearby (22 pc), bright ($V \simeq 6.9$ mag), young (414 ± 23 Myr) star that is reminiscent of a young Sun. HD 63433 d orbits its host star with a period of $4.209075^{+0.000012}_{-0.000023}$ days interior to two other previously known mini Neptunes (Mann et al. 2020). In addition, we identified a catalog of 56 likely UMa stellar members with kinematics matching the group's known motion and photometric rotation periods, consistent with its young estimated age. We reestablish membership of HD 63433 in the UMa group by showing that its color–magnitude diagram position, rotation period, lithium abundance, and kinematics are all highly consistent with these other sources.

HD 63433 d is the closest planet to our solar system with an Earth-like radius orbiting a young star. Therefore, this is an appealing target for follow-up observations, offering an opportunity to reveal insights into the physics of exoplanet atmospheric mass loss. Between HD 63433 d and the two previously known larger planets, the HD 63433 system is poised to play an important role in our understanding of planetary system evolution in the first billion years after formation.

Facilities: TESS, Gaia DR3 (Gaia Collaboration et al. 2021), Mikulski Archive for Space Telescopes (Marston et al. 2018), ROSAT, WISE, LCOGT 1 m (Sinistro), LCOGT 1 m (NRES), SMARTS 1.5 m (CHIRON), TRES, SOAR (Goodman), Telescopio Nazionale Galileo (HARPS-N), OHP 1.93 m (ELODIE), OHP 1.93 m (SOPHIE), Shane 3 m (Hamilton).

Software: AstroImageJ (Collins et al. 2017), astro-query (Ginsburg et al. 2019), BANZAI (McCully et al. 2018), batman (Kreidberg 2015), corner.py (Foreman-Mackey 2016), edmcmc (Vanderburg 2021), Lightkurve (Lightkurve Collaboration et al. 1812), matplotlib (Hunter 2007), PARSEC (Bressan et al. 2012), PyAstronomy (Czesla et al. 2019), starrotate (Angus & Garcia Soto 2023), TAPIR (Jensen 2013), TESSCUT (Brasseur et al. 2019).

ORCID iDs

Benjamin K. Capistrant ⓘ https://orcid.org/0000-0002-4592-8799
Melinda Soares-Furtado ⓘ https://orcid.org/0000-0001-7493-7419
Andrew Vanderburg ⓘ https://orcid.org/0000-0001-7246-5438
Alyssa Jankowski ⓘ https://orcid.org/0000-0003-4287-004X
Andrew W. Mann ⓘ https://orcid.org/0000-0003-3654-1602
Gabrielle Ross ⓘ https://orcid.org/0009-0006-7023-1199
Natalie R. Hinkel ⓘ https://orcid.org/0000-0003-0595-5132
Juliette Becker ⓘ https://orcid.org/0000-0002-7733-4522
Christian Magliano ⓘ https://orcid.org/0000-0001-6343-4744
Mary Anne Limbach ⓘ https://orcid.org/0000-0002-9521-9798
Alexander P. Stephan ⓘ https://orcid.org/0000-0001-8220-0548
Andrew C. Nine ⓘ https://orcid.org/0000-0002-6478-0611
Benjamin M. Tofflemire ⓘ https://orcid.org/0000-0003-2053-0749
Adam L. Kraus ⓘ https://orcid.org/0000-0001-9811-568X
Steven Giacalone ⓘ https://orcid.org/0000-0002-8965-3969
Joshua N. Winn ⓘ https://orcid.org/0000-0002-4265-047X
Allyson Bieryla ⓘ https://orcid.org/0000-0001-6637-5401
Luke G. Bouma ⓘ https://orcid.org/0000-0002-0514-5538
David R. Ciardi ⓘ https://orcid.org/0000-0002-5741-3047
Karen A. Collins ⓘ https://orcid.org/0000-0001-6588-9574
Giovanni Covone ⓘ https://orcid.org/0000-0002-2553-096X
Zoë L. de Beurs ⓘ https://orcid.org/0000-0002-7564-6047
Chelsea X. Huang ⓘ https://orcid.org/0000-0003-0918-7484
Jon M. Jenkins ⓘ https://orcid.org/0000-0002-4715-9460
Laura Kreidberg ⓘ https://orcid.org/0000-0003-0514-1147
David W. Latham ⓘ https://orcid.org/0000-0001-9911-7388
Samuel N. Quinn ⓘ https://orcid.org/0000-0002-8964-8377
Sara Seager ⓘ https://orcid.org/0000-0002-6892-6948
Avi Shporer ⓘ https://orcid.org/0000-0002-1836-3120
Joseph D. Twicken ⓘ https://orcid.org/0000-0002-6778-7552
Bill Wohler ⓘ https://orcid.org/0000-0002-5402-9613
Roland K. Vanderspek ⓘ https://orcid.org/0000-0001-6763-6562
Ricardo Yarza ⓘ https://orcid.org/0000-0003-0381-1039
Carl Ziegler ⓘ https://orcid.org/0000-0002-0619-7639

References

Aguilera-Gómez, C., Ramírez, I., & Chanamé, J. 2018, A&A, 614, A55
Akeson, R. L., Chen, X., Ciardi, D., et al. 2013, PASP, 125, 989
Ammler-von Eiff, M., Bedalov, A., Kranhold, C., et al. 2016, A&A, 591, A84
Ammler-von Eiff, M., & Guenther, E. W. 2009, A&A, 508, 677
Angus, R., & Garcia Soto, A. 2023, agarciasoto18/starrotate: Alternate Starrotate for Paper, v1.1, Zenodo, doi:10.5281/zenodo.7697238
Asphaug, E., Agnor, C. B., & Williams, Q. 2006, Natur, 439, 155
Asplund, M., Grevesse, N., Sauval, A. J., & Scott, P. 2009, ARA&A, 47, 481
Baraffe, I., Homeier, D., Allard, F., & Chabrier, G. 2015, A&A, 577, A42
Baranne, A., Queloz, D., Mayor, M., et al. 1996, A&AS, 119, 373
Barnes, S. A. 2007, ApJ, 669, 1167
Barrado, D. 2016, in EAS Publications Series, Vol. 80-81, Stellar Clusters: Benchmarks of Stellar Physics and Galactic Evolution, ed. E. Moraux, Y. D. Lebreton, & C. Charbonnel (Les Ulis: EDP Sciences), 115
Batalha, N. M., Borucki, W. J., Bryson, S. T., et al. 2011, ApJ, 729, 27
Belokurov, V., Penoyre, Z., Oh, S., et al. 2020, MNRAS, 496, 1922
Blackwell, D. E., & Shallis, M. J. 1977, MNRAS, 180, 177
Boesgaard, A. M., & Tripicco, M. J. 1986, ApJL, 302, L49
Bouvier, J., Barrado, D., Moraux, E., et al. 2018, A&A, 613, A63
Bouwman, J., Kendrew, S., Greene, T. P., et al. 2023, PASP, 135, 038002
Brasseur, C. E., Phillip, C., Fleming, S. W., Mullally, S. E., & White, R. L. 2019 Astrocut: Tools for creating cutouts of TESS images, Astrophysics Source Code Library, ascl:1905.007
Bressan, A., Marigo, P., Girardi, L., et al. 2012, MNRAS, 427, 127
Brown, T. M., Baliber, N., Bianco, F. B., et al. 2013, PASP, 125, 1031
Chambers, J. E., & Wetherill, G. W. 1998, Icar, 136, 304
Chatterjee, S., Ford, E. B., Matsumura, S., & Rasio, F. A. 2008, ApJ, 686, 580

Chen, J., & Kipping, D. 2016, ApJ, 834, 17
Ciardi, D. R., Beichman, C. A., Horch, E. P., & Howell, S. B. 2015, ApJ, 805, 16
Collins, K. A., Kielkopf, J. F., Stassun, K. G., & Hessman, F. V. 2017, AJ, 153, 77
Cowan, N. B., & Agol, E. 2011, ApJ, 726, 82
Crossfield, I. J. M., Malik, M., Hill, M. L., et al. 2022, ApJL, 937, L17
Cummings, J. D., Deliyannis, C. P., Maderak, R. M., & Steinhauer, A. 2017, AJ, 153, 128
Czesla, S., Schröter, S., Schneider, C. P., et al. 2019, PyA: Python astronomy-related packages, Astrophysics Source Code Library, ascl:1906.010
Dai, F., Roy, A., Fulton, B., et al. 2020, AJ, 160, 193
Damasso, M., Locci, D., Benatti, S., et al. 2023, A&A, 672, A126
Douglas, S. T., Agüeros, M. A., Covey, K. R., et al. 2016, ApJ, 822, 47
Douglas, S. T., Agüeros, M. A., Covey, K. R., & Kraus, A. 2017, ApJ, 842, 83
Evans, D. F. 2018, RNAAS, 2, 20
Fabrycky, D., & Tremaine, S. 2007, ApJ, 669, 1298
Fabrycky, D. C., Ford, E. B., Steffen, J. H., et al. 2012, ApJ, 750, 114
Fűrész, G. 2008, PhD thesis, University of Szeged
Fischer, D. A., Marcy, G. W., & Spronck, J. F. P. 2014, ApJS, 210, 5
Ford, E. B., & Rasio, F. A. 2008, ApJ, 686, 621
Foreman-Mackey, D. 2016, JOSS, 1, 24
Fortney, J. J., Ikoma, M., Nettelmann, N., Guillot, T., & Marley, M. S. 2011, ApJ, 729, 32
Fregeau, J. M., Chatterjee, S., & Rasio, F. A. 2006, ApJ, 640, 1086
Fulton, B. J., Petigura, E. A., Howard, A. W., et al. 2017, AJ, 154, 109
Gagné, J., Faherty, J. K., & Popinchalk, M. 2020, RNAAS, 4, 92
Gagné, J., Mamajek, E. E., Malo, L., et al. 2018, ApJ, 856, 23
Gaia Collaboration, Brown, A. G. A., Vallenari, A., et al. 2021, A&A, 649, A1
Gaia Collaboration 2022, yCat, I/355
Gelman, A., & Rubin, D. B. 1992, StaSc, 7, 457
Giacalone, S., Dressing, C. D., Jensen, E. L. N., et al. 2021, AJ, 161, 24
Ginsburg, A., Sipőcz, B. M., Brasseur, C. E., et al. 2019, AJ, 157, 98
Ginzburg, S., Schlichting, H. E., & Sari, R. 2018, MNRAS, 476, 759
Gladman, B., Quinn, D. D., Nicholson, P., & Rand, R. 1996, Icar, 122, 166
Gonzalez, G., Carlson, M. K., & Tobin, R. W. 2010, MNRAS, 403, 1368
Gray, R. O., Corbally, C. J., Garrison, R. F., McFadden, M. T., & Robinson, P. E. 2003, AJ, 126, 2048
Greene, T. P., Bell, T. J., Ducrot, E., et al. 2023, Natur, 618, 39
Guerrero, N. M., Seager, S., Huang, C. X., et al. 2021, ApJS, 254, 39
Gupta, A., & Schlichting, H. E. 2019, MNRAS, 487, 24
Hansen, B. M. S. 2009, ApJ, 703, 1131
Harre, J.-V., & Heller, R. 2021, AN, 342, 578
Hartman, J. D., Bakos, G. Á., Kovács, G., & Noyes, R. W. 2010, MNRAS, 408, 475
Hinkel, N. R., Timmes, F. X., Young, P. A., Pagano, M. D., & Turnbull, M. C. 2014, AJ, 148, 54
Hippke, M., & Heller, R. 2019, A&A, 623, A39
Huang, C. X., Vanderburg, A., Pál, A., et al. 2020a, RNAAS, 4, 204
Huang, C. X., Vanderburg, A., Pál, A., et al. 2020b, RNAAS, 4, 206
Huber, D., White, T. R., Metcalfe, T. S., et al. 2022, AJ, 163, 79
Hunter, J. D. 2007, CSE, 9, 90
Jeffries, R. D. 2014, in EAS Publications Series, Vol. 65, The Ages of Stars, ed. Y. Lebreton, D. Valls-Gabaud, & C. Charbonnel (Les Ulis: EDP Sciences), 289
Jenkins, J. M., Twicken, J. D., McCauliff, S., et al. 2016, Proc. SPIE, 9913, 99133E
Jensen, E., 2013 Tapir: A web interface for transit/eclipse observability, Astrophysics Source Code Library, ascl:1306.007
Johnson, D. R. H., & Soderblom, D. R. 1987, AJ, 93, 864
Jones, J., White, R. J., Boyajian, T., et al. 2015, ApJ, 813, 58
Kempton, E. M. R., Bean, J. L., Louie, D. R., et al. 2018, PASP, 130, 114401
King, J. R., & Schuler, S. C. 2005, PASP, 117, 911
Kipping, D. M. 2013, MNRAS, 435, 2152
Kovács, G., Zucker, S., & Mazeh, T. 2002, A&A, 391, 369
Kreidberg, L. 2015, PASP, 127, 1161
Kreidberg, L., Koll, D. D. B., Morley, C., et al. 2019, Natur, 573, 87
Lammer, H., Selsis, F., Ribas, I., et al. 2003, ApJL, 598, L121
Léger, A., Rouan, D., Schneider, J., et al. 2009, A&A, 506, 287
Lightkurve Collaboration, Cardoso, J. V. d. M., Hedges, C., et al., 1812 Lightkurve: Kepler and TESS time series analysis in Python, Astrophysics Source Code Library, ascl:1812.013
Llorente de Andrés, F., Chavero, C., de la Reza, R., Roca-Fàbrega, S., & Cifuentes, C. 2021, A&A, 654, A137
Lomb, N. R. 1976, Ap&SS, 39, 447

Lopez, E. D., & Fortney, J. J. 2013, ApJ, 776, 2
Luck, R. E. 2017, AJ, 153, 21
Mallorquín, M., Béjar, V. J. S., Lodieu, N., et al. 2023, A& A, 671, A163
Mann, A. W., Johnson, M. C., Vanderburg, A., et al. 2020, AJ, 160, 179
Mann, A. W., Newton, E. R., Rizzuto, A. C., et al. 2016, AJ, 152, 61
Marston, A., Hargis, J., Levay, K., et al. 2018, Proc. SPIE, 10704, 1070413
Masci, F. J., Laher, R. R., Rusholme, B., et al. 2019, PASP, 131, 018003
Mason, B. D., Wycoff, G. L., Hartkopf, W. I., Douglass, G. G., & Worley, C. E. 2001, AJ, 122, 3466
McCully, C., Volgenau, N. H., Harbeck, D.-R., et al. 2018, Proc. SPIE, 10707, 107070K
McQuillan, A., Aigrain, S., & Mazeh, T. 2013, MNRAS, 432, 1203
Meibom, S., Barnes, S. A., Latham, D. W., et al. 2011, ApJL, 733, L9
Miczaika, G. R. 1948, LicOB, 20, 83
Mishenina, T. V., Soubiran, C., Bienaymé, O., et al. 2008, A&A, 489, 923
Morbidelli, A., Lunine, J. I., O'Brien, D. P., Raymond, S. N., & Walsh, K. J. 2012, AREPS, 40, 251
Morris, R. L., Twicken, J. D., Smith, J. C., et al. 2020, Kepler Data Processing Handbook: Photometric Analysis KSCI-19081-003, Kepler Science Document
Morton, T. D. 2012, ApJ, 761, 6
Morton, T. D., 2015 VESPA: False positive probabilities calculator, Astrophysics Source Code Library, record, ascl:1503.011
Mucciarelli, A., Bellazzini, M., & Massari, D. 2021, A&A, 653, A90
Naoz, S., Farr, W. M., Lithwick, Y., Rasio, F. A., & Teyssandier, J. 2011, Natur, 473, 187
Newton, E. R., Mann, A. W., Tofflemire, B. M., et al. 2019, ApJL, 880, L17
NExScI 2022, Exoplanet Follow-up Observing Program Web Service, IPAC, doi:10.26134/EXOFOP5
Owen, J. E., & Wu, Y. 2013, ApJ, 775, 105
Owen, J. E., & Wu, Y. 2017, ApJ, 847, 29
Pepper, J., Kane, S. R., Rodriguez, J. E., et al. 2020, AJ, 159, 243
Perruchot, S., Kohler, D., Bouchy, F., et al. 2008, Proc. SPIE, 7014, 70140J
Raghavan, D., Farrington, C. D., ten Brummelaar, T. A., et al. 2012, ApJ, 745, 24
Ramírez, I., Fish, J. R., Lambert, D. L., & Allende Prieto, C. 2012, ApJ, 756, 46
Rebull, L. M., Stauffer, J. R., Bouvier, J., et al. 2016, AJ, 152, 113
Ricker, G. R., Winn, J. N., Vanderspek, R., et al. 2015, JATIS, 1, 014003
Rizzuto, A. C., Vanderburg, A., Mann, A. W., et al. 2018, AJ, 156, 195
Rogers, L. A. 2015, ApJ, 801, 41
Ross, G., Vanderburg, A., de Beurs, Z., et al. 2023, MNRAS, in press
Rowe, J. F., Bryson, S. T., Marcy, G. W., et al. 2014, ApJ, 784, 45
Santos, N. C. 2008, NewAR, 52, 154
Scargle, J. D. 1982, ApJ, 263, 835
Schwarzenberg-Czerny, A. 1997, ApJ, 489, 941
Siverd, R. J., Brown, T. M., Barnes, S., et al. 2018, Proc. SPIE, 10702, 107026C
Skumanich, A. 1972, ApJ, 171, 565
Smith, J. C., Stumpe, M. C., Van Cleve, J. E., et al. 2012, PASP, 124, 1000
Soderblom, D. R., Pilachowski, C. A., Fedele, S. B., & Jones, B. F. 1993, AJ, 105, 2299
Stellingwerf, R. F. 1978, ApJ, 224, 953
Stumpe, M. C., Smith, J. C., Catanzarite, J. H., et al. 2014, PASP, 126, 100
Stumpe, M. C., Smith, J. C., Van Cleve, J. E., et al. 2012, PASP, 124, 985
Ter Braak, C. J. F. 2006, S&C, 16, 239
Tofflemire, B. M., Rizzuto, A. C., Newton, E. R., et al. 2021, AJ, 161, 171
Twicken, J. D., Catanzarite, J. H., Clarke, B. D., et al. 2018, PASP, 130, 064502
Twicken, J. D., Clarke, B. D., Bryson, S. T., et al. 2010, Proc. SPIE, 7740, 774023
Van Eylen, V., Agentoft, C., Lundkvist, M. S., et al. 2018, MNRAS, 479, 4786
Van Eylen, V., Albrecht, S., Huang, X., et al. 2019, AJ, 157, 61
van Saders, J. L., Ceillier, T., Metcalfe, T. S., et al. 2016, Natur, 529, 181
Vanderburg, A. 2021, avanderburg/edmcmc: v1.0.0, Zenodo, doi:10.5281/zenodo.5599854
Vanderburg, A., Huang, C. X., Rodriguez, J. E., et al. 2019, ApJL, 881, L19
Vanderburg, A., Latham, D. W., Buchhave, L. A., et al. 2016, ApJS, 222, 14
von Braun, K., Boyajian, T. S., Kane, S. R., et al. 2012, ApJ, 753, 171
Zechmeister, M., & Kürster, M. 2009, A&A, 496, 577
Zeng, L., Jacobsen, S. B., Sasselov, D. D., et al. 2019, PNAS, 116, 9723
Zhang, M., Knutson, H. A., Wang, L., et al. 2022, AJ, 163, 68
Zieba, S., Kreidberg, L., Ducrot, E., et al. 2023, Natur, 620, 746